UNIVERSITÀ DEGLI STUDI DI BERGAMO
DIPARTIMENTO DI INGEGNERIA DELL'INFORMAZIONE
E METODI MATEMATICI°

QUADERNI DEL DIPARTIMENTO

Department of Information Technology and Mathematical Methods

Working Paper

Series "*Mathematics and Statistics*"

n. 6/MS – 2010

A variational approach for estimating the compliance of the cardiovascular tissue: An inverse fluid-structure interaction problem

by

M. Perego, A. Veneziani, C. Vergara

° Viale Marconi. 5, I – 24044 Dalmine (BG), ITALY, Tel. +39-035-2052339; Fax. +39-035-562779

COMITATO DI REDAZIONE[§]

Series Information Technology (IT): Stefano Paraboschi
Series Mathematics and Statistics (MS): Luca Brandolini, Ilia Negri

[§] L'accesso alle *Series* è approvato dal Comitato di Redazione. I *Working Papers* della Collana dei Quaderni del Dipartimento di Ingegneria dell'Informazione e Metodi Matematici costituiscono un servizio atto a fornire la tempestiva divulgazione dei risultati dell'attività di ricerca, siano essi in forma provvisoria o definitiva.

A VARIATIONAL APPROACH FOR ESTIMATING THE COMPLIANCE OF THE CARDIOVASCULAR TISSUE: AN INVERSE FLUID-STRUCTURE INTERACTION PROBLEM

MAURO PEREGO , ALESSANDRO VENEZIANI*, AND CHRISTIAN VERGARA†

Abstract. Estimation of the stiffness of a biological soft tissue is useful for the detection of pathologies such as tumors or atherosclerotic plaques. *Elastography* is a method based on the comparison between two images before and after a forced deformation of the tissue of interest. An inverse elasticity problem is then solved for the Young modulus estimation. In the case of arteries, no forced deformation is required, since vessels naturally move under the action of blood. Young modulus can be therefore estimated by solving a coupled inverse fluid-structure interaction problem. In this paper we focus on the mathematical properties of this problem and its numerical solution. We give some well posedness analysis and some preliminary results based on a synthetic data-set, i.e. test cases where the exact Young modulus is known and the displacement dataset is numerically generated by solving a forward fluid-structure interaction problem. We address the problem of the presence of the noise in the measured displacement and of the proper sampling frequency for obtaining reliable estimates.

Key words. Fluid-structure Interaction, Inverse Problems, Parameter Estimation

1. Introduction. The term *compliance* in physiology is referred to the tendency of a vessel or more in general a hollow organ to resist recoil toward its original dimension when a distending or compressing force is removed. A practical definition of compliance is the ratio between the volume variation in a vessel and the corresponding pressure variation (see e.g. [30]). Nevertheless, there are different definitions of compliance, mainly dependent of the different methods for measuring it.

This parameter is supposed to have a role in different cardiovascular pathologies, so its estimation is a major issue in clinical diagnosis and therapy. For example, low compliance of a artery vessel could be an indicator of atherosclerosis or hypertension (see e.g. [20], Chapter 28, and [11], Chapter 5). Moreover, an increase of the stiffness of the left ventricle wall is a clear marker of *diastolic dysfunction*, i.e a clinical condition leading to an increase of the end diastolic left ventricle pressure, that may be the *primum movens* of heart failure (see e.g. [20], Chapter 15, and [11], Chapter 79). More in general, the deformability of soft tissues is an important index for the detection of anomalies or diseases such as tumors. For all these reasons, an accurate estimation of this parameter *in vivo* has a great relevance for diagnostic purposes and however it is difficult for many reasons. As stated in the pioneering work [8], "a practical method of measuring the compliance of the arterial system in both patients and healthy individuals must meet the following requirements at least: it must be relatively simple, safe and should cause minimal discomfort to the subject." Among the techniques specifically devised for the vascular compliance, we mention (see [36]) 1) Methods based on the simultaneous measures of pressure and cross-sectional area at different points and times [46]; 2) Methods based on measuring the rate of propagation of flow waves coming form the heart (*pulse wave velocity*) [3, 49]. The former has a major drawback in its invasivity. The latter requires a specific attention in handling pressure wave reflections (see [49]) and relies upon the assumption of cylindrical vessels, which is not true in general.

*Department of Mathematics and Computer Science, Emory University, Atlanta, Georgia, USA, <mauro,ale@mathcs.emory.edu>

†Dipartimento di Ingegneria dell'Informazione e Metodi Matematici, Università di Bergamo, Italy, christian.vergara@unibg.it

Other methods were proposed for more general purposes, in particular for the detection of tumors in a soft tissue. In particular, *elastography* is an approach where tissue elasticity (or stiffness) is inferred by the analysis of images of the tissue before and after the application of a proper deformation (see e.g. [34, 33, 43, 2]). Images are in general acquired with ultrasound or magnetic resonance. Basic steps of this approach are: (i) *First acquisition* of the specimen in the original configuration; (ii) Application of a deformation to the specimen and *second acquisition*; (iii) *Tracking* of the displacement from the comparison between the two images; (iv) *Estimation* of the rigidity of the tissue. Both steps (iii) and (iv) require the solution of inverse problems. Step (iii) is actually an *image registration* step [15] for retrieving the displacement field. Step (iv) entails the solution of what has been called the *inverse elasticity problem*. The shear modulus or the Young modulus of the tissue, assumed to be linearly elastic, is estimated by minimizing the mismatch between the measures (displacement field) and the solution of an appropriate elasticity problem. More recently, in [35] a similar approach has been proposed to evaluate the Young modulus of mandibular bone. In general, the problem of estimating the parameters of a partial differential equation has been pursued in [5, 48, 7] for the diffusion coefficient in the elliptic case and in [26] for the convective heat transfer coefficent in the heat equation.

The present work follows a similar approach specifically devised for vessel compliance. As a matter of fact, for our purpose the specificity of vessels is that they do not need an externally forced deformation, since blood pulsatility naturally induces vessel motion. The latter can be retrieved from time frames of the vessel of interest and proper measurements of blood velocity and pressure. No particular devices or protocols are therefore needed in our approach different from a routine 4D scan of a patient. The methodological drawback here is that the deformation is not known *a priori* but it is induced by blood. For this reason, the inverse problem to be solved for the parameter estimation is not simply an elasticity model, but a fully coupled fluid-structure interaction (FSI) system. Some steps in this direction have been carried out in [27] where however the FSI problem was one-dimensional. In [28] a coefficient estimation of the 1D model was based on the minimization of the differences with a 3D computation.

In summary, our approach for estimating compliance is as follows (see Fig. 1).

Retrieval of the vessel displacement $\boldsymbol{\eta}_{meas}$ by image registration procedures on time frames of the vessel of interest (see e.g. [40] where images acquired with a Siemens©SOMATOM are used with a frequency of 65 frames per heart beat). Reliability of our approach relies also upon the availability of measures of blood velocity and pressure to be used as boundary conditions in the second step.

Minimization of the difference between $\boldsymbol{\eta}_{meas}$ and the displacement computed by solving the coupled 3D blood-vessel problem, to estimate the Young modulus.

In this paper we focus on the second step, which is an example of an *inverse fluid-structure interaction* (IFSI) problem. The corresponding forward mathematical problem, the 3D fluid-structure interaction (FSI) system, has been considered in numerical haemodynamics simulations since many years (see e.g. Perktold and his co-workers, [39, 38]). This is still a challenging problem both under the view point of mathematical analysis and numerical solution. Relevant contribution have been given by different authors (see e.g. [10, 41, 47, 6, 9, 14, 50]). The recent reviews in the book [16] by Y. Maday (Chapter 8) and J.F. Gerbeau and M. Fernandez (Chapter 9) give an up-to-date picture of the current research in this field. Examples of

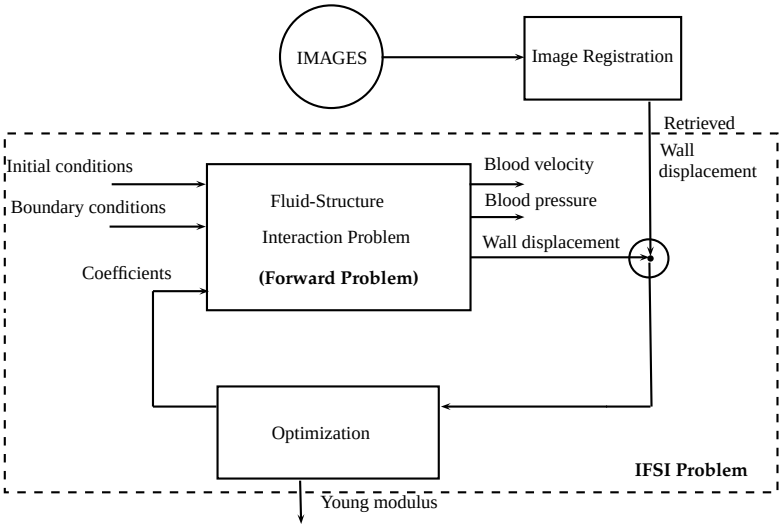

FIG. 1.1. *Scheme of the proposed approach*

inverse problems addressing a fully coupled FSI problem are analyzed in [29], where the minimization of a functional involving measured and computed fluid velocity and structure displacement is considered.

The purpose of this paper is to perform preliminary analysis of the IFSI problem when the structure is assumed to be linearly elastic and the only parameter to be estimated is the Young modulus. The same approach in principle can be adopted with more complex structure models (see e.g. [23]) and with more parameters to be estimated. In particular, we discuss different approaches for tackling with IFSI problem. This is a 4D optimization problem. Different strategies can be followed for its solution depending on the order of the optimization and discretization steps. We focus on an approach where the original problem is first discretized in time, then the optimization step is performed. The well posedness of the resulting IFSI problem is analyzed. Possible numerical methods for its solution are then introduced. In this first work, numerical results presented refer to 2D and 2D axisymmetric test cases, where synthetic data (that is obtained by a forward FSI problem) are considered, aiming at a general assessment of the methodology. More complex test cases referring to real geometries will be presented elsewhere. Finally, it is worth mentioning that an IFSI problem with different control variables has been considered in [17], as a step for prescribing flow rates to the blood flow problem in compliant domains.

There are two relevant concerns that need to be addressed at this stage.

1. *Sampling frequency.* Displacement is retrieved at instants driven by the acquisition device. More data are available and more accurate is supposed to be the estimate of the compliance. A careful analysis of the impact of this sampling frequency on the reliability of the entire process is however a major issue.
2. *Noise.* Measurements are affected by errors and noise, introduced by both the acquisition and the registration. A precise quantification of the impact of the noise with realistic acquisition devices to the final estimate is beyond the purpose of the present paper. However, in the synthetic numerical simulations we will investigate the impact of possible uncertainties to the reliability of the

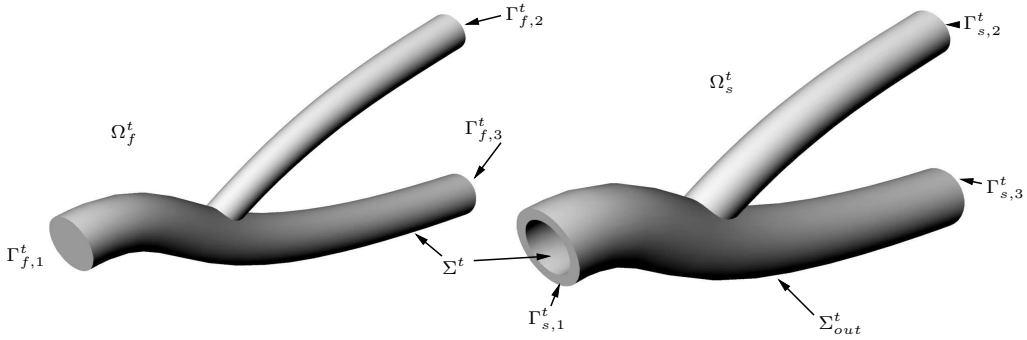

FIG. 2.1. *Representation of the domain of the IFSI problem: fluid domain on the left, structure domain on the right.*

entire method, for drawing preliminary conclusions on their relevance.

The outline of the paper is as follows. In Sect. 2 we address the forward FSI problem considered, both in strong and weak formulation, and we recall the basic properties of the solution to this problem. Moreover, we introduce the general setting of the IFSI problem and an approach for its solution (Karush-Kuhn-Tucker (KKT) conditions). Well posedness analysis of the IFSI problem is carried out in Sect. 3. Numerical method for the solution are presented in Sect. 4, whilst numerical results are presented and discussed in Sect. 5. Finally, in Sect. 6 we deal with a simplified structure model which leads to a significant reduction of the computational time.

2. The IFSI Problem.

2.1. The forward problem. Let us consider the domain $\Omega^t_f \subset \mathbb{R}^d$ (d=2, 3, being the space dimension) represented in Fig. 2.1 (on the left). This represents the lumen of a vessel and it is function of time t. Inflow and outflow sections are denoted by $\Gamma^t_{f,i}$ where $i = 1, \ldots, N_s$ and N_s is the number of sections (three in Figure 2.1). Blood velocity is denoted by $\boldsymbol{u}(\boldsymbol{x}, t)$, the pressure by $p(\boldsymbol{x}, t)$. The incompressible Navier-Stokes equations for a Newtonian fluid are assumed to hold in Ω^t_f. Since we work in a moving domain, the fluid problem is stated in an *Arbitrary Lagrangian-Eulerian* (ALE) framework (see e.g. [25, 10]). The ALE mapping is defined by an appropriate lifting of the structure displacement at the FS interface Σ^t. A classical choice is to consider a harmonic extension operator in the reference domain, which defines the velocity of the points of the fluid domain $\boldsymbol{w}$.

The vessel wall is denoted by Ω^t_s, which is still a subset of $\mathbb{R}^d$ (see Fig. 2.1, right). The intersection of Ω^t_s and Ω^t_f is empty, their union is called Ω^t. The vascular wall is assumed to obey the equations of a linear elastic material. As mentioned above, more complex constitutive laws where the parameters can be used as control variables in the optimization process could be a possible development of this work. As for the fluid, the inflow/outflow sections (three in Fig. 2.1) are denoted by $\Gamma^t_{s,i}$. With Σ^t_{out} we denote the external surface of the structure domain.

If we denote by $\boldsymbol{\eta}(\boldsymbol{x}, t)$ the wall displacement with respect to a reference configuration, the Cauchy stress tensor for the wall will be

$$\boldsymbol{T}_s(\boldsymbol{\eta}) := \gamma_1(\nabla\boldsymbol{\eta} + (\nabla\boldsymbol{\eta})^T) + \gamma_2(\nabla \cdot \boldsymbol{\eta})\boldsymbol{I},$$

where

$$\gamma_1 := \frac{E}{2(1+\nu)}, \qquad \gamma_2 := \frac{E\nu}{(1+\nu)(1-2\nu)},$$

are the Lamé constants, $\boldsymbol{I}$ is the identity tensor, E is the Young modulus and ν is the Poisson ratio. For the sake of notation, we set

$$\boldsymbol{S}_s(\boldsymbol{\eta}) = \frac{1}{2(1+\nu)}(\nabla\boldsymbol{\eta} + (\nabla\boldsymbol{\eta})^T) + \frac{\nu}{(1+\nu)(1-2\nu)}(\nabla\cdot\boldsymbol{\eta})\boldsymbol{I}$$

so that we can write $\boldsymbol{T}_s = E\,\boldsymbol{S}_s$. The compliance of the vessel is completely described by the Young modulus E, which is in general a function of space (e.g. an atherosclerotic plaque has different modulus than healthy tissue) and time (in the heart, see [24]). The Young modulus is the parameter we want to estimate, so we will use it as control variable in the optimization process. Specific assumptions on E will be postulated later on. To describe the structure kinematics we adopt a purely Lagrangian approach. Moreover, we assume the displacements to be small, so that the constitutive law is referred to the reference domain $\Omega_s := \Omega_s^0$. Consederably, we drop index t when referring to structure domain and boundary. For any function g defined in the reference solid configuration, we denote by $\widehat{g}$ its counterpart in the current domain.

The two subproblems are coupled by the interface conditions, stating the continuity of the velocity and stress fields. The strong formulation of the FSI forward problem, including the computation of the arbitrary extension in the fluid domain of the FS interface structure displacement, reads therefore as follows ($\boldsymbol{n}$ is the outward unit vector normal to the associated part of $\partial\Omega_s^t$).

1. *Fluid-Structure problem.* Find fluid velocity $\boldsymbol{u}$, pressure p and structure displacement $\boldsymbol{\eta}$ such that

$$\begin{cases} \rho_f \dfrac{D^A\boldsymbol{u}}{Dt} + \rho_f((\boldsymbol{u}-\boldsymbol{w})\cdot\nabla)\boldsymbol{u} - \nabla\cdot\boldsymbol{T}_f = \boldsymbol{f}_f & \text{in } \Omega_f^t\times(0,T), \\ \nabla\cdot\boldsymbol{u} = 0 & \text{in } \Omega_f^t\times(0,T), \\ \rho_s \dfrac{\partial^2\boldsymbol{\eta}}{\partial t^2} - \nabla\cdot(E\,\boldsymbol{S}_s) = \boldsymbol{f}_s & \text{in } \Omega_s\times(0,T), \\ \boldsymbol{u} = \frac{\partial\widehat{\boldsymbol{\eta}}}{\partial t} & \text{on } \Sigma^t\times(0,T), \\ \widehat{\boldsymbol{T}}_s\,\boldsymbol{n} - \boldsymbol{T}_f\,\boldsymbol{n} = \boldsymbol{0} & \text{on } \Sigma^t\times(0,T), \\ \boldsymbol{T}_s\,\boldsymbol{n} = \boldsymbol{0}, & \text{on } \Sigma_{out}\times(0,T), \end{cases} \tag{2.1}$$

   where $\widehat{\boldsymbol{T}}_s := \boldsymbol{T}_s(\widehat{\boldsymbol{\eta}})$ and $\boldsymbol{T}_f(\boldsymbol{u},p) = -p\boldsymbol{I} + \mu(\nabla\boldsymbol{u} + (\nabla\boldsymbol{u})^T)$;
2. *Geometry problem.* Given the interface structure displacement $\boldsymbol{\eta}|_\Sigma$, find a map $\mathcal{A}:\Omega_f^0\to\Omega_f^t$ through an harmonic extension Ext of this boundary value and find accordingly the new fluid domain Ω_f^t by moving the point $\boldsymbol{x}_0$ of the reference domain Ω_f^0:

$$\mathcal{A}^t(\boldsymbol{x}_0) = \boldsymbol{x}_0 + \mathrm{Ext}(\boldsymbol{\eta}|_{\Sigma^0}), \quad \boldsymbol{w} = \partial_t\mathcal{A}^t\circ(\mathcal{A}^t)^{-1}, \quad \Omega_f^t = \mathcal{A}^t(\Omega_f^0). \tag{2.2}$$

Here, ρ_f and ρ_s are the fluid and structure density, μ is the constant blood viscosity, $\boldsymbol{f}_f$ and $\boldsymbol{f}_s$ the forcing terms. The two matching conditions enforced at the interface are $(2.1)_4$ (*continuity of fluid and structure velocities*) and $(2.1)_5$ (*continuity of stresses*). The fluid and structure are also coupled by the geometry problem, leading to a highly nonlinear system of partial differential equations. System (2.1) has to

be endowed with suitable boundary conditions on $\Omega_f^t \setminus \Sigma^t$ and $\Omega_s \setminus (\Sigma \cup \Sigma_{out})$, and with suitable initial conditions. We prescribe a free-stress condition on Σ_{out}, however, other boundary conditions could be considered as well for including the presence of surrounding tissues. For the inflow/outflow sections, several papers discuss possible reliable conditions in haemodynamics: in this respect, see the recent review in [16], Chapter 11. In particular we prescribe natural conditions for the structure and either Dirichlet conditions or natural conditions, depending on the data availability (blood velocity or pressure), for the fluid. The correct prescription of these conditions is crucial for the reliability of the parameter estimation *in vivo*. However, from the methodological viewpoint different conditions do not introduce significant changes, so we do not dwell with this aspect any longer.

2.2. The time-continuous inverse problem. Let us assume that the displacement data retrieved from the image registration process are available within the interval $[0, T]$ in some instants denoted by τ_k, $k = 1, \ldots, N$ (N being the number of instants when image registration is performed). It is realistic and not restrictive to assume that the time step between two measurement instants is constant. It will be denoted by $\Delta\tau$. This is actually driven by the sampling frequency of the image devices. Let $\hat{\boldsymbol{\eta}}_{meas}(\boldsymbol{x}, \tau_k)$ be the measured displacement at τ_k for $\boldsymbol{x} \in \Sigma^{\tau_k}$. We introduce the following functional

$$\mathcal{J}_c = \frac{1}{2} \sum_{k=1}^{N} \int_{\Sigma} \left(\boldsymbol{\eta}_{meas}(\boldsymbol{x}, \tau_k) - \boldsymbol{\eta}(\boldsymbol{x}, \tau_k)\right)^2 d\sigma.$$

where $\boldsymbol{\eta}(\boldsymbol{x}, \tau_k)$ solves equations (2.1) at instants τ_k. We may consider the functional

$$\mathcal{J}_c^{\mathcal{R}} = \mathcal{J}_c + \mathcal{R}_c(E)$$

where $\mathcal{R}_c(E)$ is a non-negative regularization term depending on the regularity assumptions on E. Given an admissible set $\mathcal{E}_{ad}$ for the control variable E, a first possible formulation of the IFSI problem reads:

PROBLEM 1. *For $t > 0, \boldsymbol{x} \in \Omega_s$, find $E = E(\boldsymbol{x}, t) \in \mathcal{E}_{ad}$ that minimizes the functional $\mathcal{J}_c^{\mathcal{R}}$ under the constraint* (2.1).

The term $\mathcal{E}_{ad}$ is the set where we are looking for the minimum. In the following, unless stated otherwise, we define $\mathcal{E}_{ad}$ as:

$$\mathcal{E}_{ad} := \{E : E \in L^\infty(\Omega_s),\, 0 < E_{min} \leq E \leq E_{max}, \text{with } E_{min}, E_{max} \in \mathbb{R}\}. \tag{2.3}$$

REMARK 1. *The term $\mathcal{R}_c$ can be the usual Tychonov regularization, which is expected to force better mathematical and numerical properties to the minimization process. As an example, it could be defined as*

$$\mathcal{R}_c(E) = \frac{\xi}{2} \sum_{k=1}^{N} \int_{\Omega_s} \left(E(\boldsymbol{x}, \tau_k) - E_{ref}\right)^2 d\boldsymbol{x},$$

where E_{ref} is a reference value (available for instance from ex vivo specimens). In this case, the regularization is forcing the value of E to be close to the reference value. Parameter ξ weights the relevance of the regularization in the minimization procedure and can be tuned empirically on the basis of the Morozov's discrepancy principle (see e.g. [12]).

REMARK 2. *The minimization of the mismatch between measured and computed displacement fields is performed over the interface between the fluid and the structure domain. This choice is basically motivated by the fact that usually this is clearly visible in the images (due to the high contrast of the difference in the grey levels of the two regions) so the retrieved displacement on the interface is expected to be more correct. This is however just one possible choice driven by technical limitation of the image acquisition. Should clear images of the vessel wall be available, minimization of the mismatch can be performed over the entire structure domain* Ω_s.

Problem 1 entails the solution of a time-dependent minimization problem. A possible approach for the solution is the introduction of *Lagrange multipliers* for the constraints given by (2.1) and (2.2) and of a functional (Lagrangian) to be minimized without constraints. This functional is then differentiated with respect to the state variables (blood velocity and pressure, and structure displacement), the multipliers and the control variable E, so to obtain the classical KKT system (state problem, adjoint problem, optimality conditions).

This approach is expected to suffer from two major drawbacks.

1. *Complexity.* The adjoint of an initial value problem is a final value problem so that, in principle, solution requires to handle a genuine 4D coupled problem (for three space dimensions), which is expensive. Moreover, the constraint is represented by a moving domain problem, where the shape of the domain is unknown. In computing the adjoint problem, differentiation with respect to the domain (*shape derivative*) needs to be performed, that is in general fairly expensive too.
2. *Storage.* Even if at the numerical level splitting techniques can overcome the solution of a fully 4D problem, still the solution at all the time steps needs typically to be stored, with a massive memory occupancy.

For all these reasons we resort to a different formulation of the problem where dependence on time is discretized *before* the formulation of the minimization problem.

2.3. The time-discrete forward problem. Let us consider the time discretization of the fluid-structure interaction problem (2.1). For the sake of simplicity we assume a constant time step Δt such that

$$\Delta t = \frac{\Delta \tau}{s} \quad \text{with } \mathbb{N} \ni s \geq 1.$$

In other words, the measurements instants τ_k are a subset of the time discretization of (2.1). This is not restrictive, since numerical arguments (stability, accuracy) usually force to use time steps smaller than the acquisition interval of current devices. Should instants τ_k do not coincide with time discretization nodes, suitable interpolation procedures need to be introduced for computing the difference between measurements and numerical simulations. These (standard) procedures do not change the core of the procedure we address in this work.

We set $t^n = n\Delta t$ for $n = 0, \ldots, N$ and denote by z^n the approximation of a generic time dependent function z at time level t^n. For the time discretization of (2.1) we resort basically to an implicit Euler scheme for first order differential problems in time and BDF schemes for second order time derivatives. Observe, however, that all the arguments detailed in this work can be extended to other time discretization schemes. More precisely, a *semi-implicit* approximation is considered (see e.g. [14, 1]) for the fluid problem for tackling with the nonlinearities induced by the convective term and

by the moving domain. Differently from [14] we treat implicitely the fluid viscous term. Denote by $\Omega_f^\star$, $\boldsymbol{u}^\star$ and $\boldsymbol{w}^\star$ appropriate extrapolations of the fluid domain, fluid velocity and fluid domain velocity, respectively. The simplest choice is given by the first order extrapolations $\Omega_f^\star = \Omega_f^n$, $\boldsymbol{u}^\star = \boldsymbol{u}^n$ and $\boldsymbol{w}^\star = \boldsymbol{w}^n$.

Since we resort to Finite Element space discretizations we introduce directly the weak formulation of the time-discrete fluid-structure interaction problem. The following spaces will be useful,

$$\boldsymbol{V}^\star = \{\boldsymbol{v} \in \boldsymbol{H}^1(\Omega_f^\star) : \boldsymbol{v}|_{\Gamma_{D,f}^\star} = \boldsymbol{0}\},\ Q^\star = L^2(\Omega_f^\star),\ \boldsymbol{W} = \{\boldsymbol{\psi} \in \boldsymbol{H}^1(\Omega_s) : \boldsymbol{\psi}_{\Gamma_{D,s}} = \boldsymbol{0}\},$$

where $\Gamma_{D,f}^\star$ and $\Gamma_{D,s}$ are the portions of the boundary where a Dirichlet condition is prescribed. We denote moreover $\boldsymbol{Z}^\star = \left\{(\boldsymbol{v},\boldsymbol{\psi}) \in \boldsymbol{V}^\star \times \boldsymbol{W} : \boldsymbol{v}|_{\Sigma^\star} - \frac{\widehat{\boldsymbol{\psi}}|_{\Sigma^\star}}{\Delta t} = \boldsymbol{0}\right\}$. Then we set

$$\begin{aligned} a(\boldsymbol{u},\boldsymbol{\eta};\boldsymbol{v},\boldsymbol{\psi})^\star &:= \tfrac{\rho_f}{\Delta t}\,(\boldsymbol{u},\boldsymbol{v})_f^\star + (\boldsymbol{T}_f(\boldsymbol{u},p),\nabla\boldsymbol{v})_f^\star + \rho_f(((\boldsymbol{u}^\star - \boldsymbol{w}^\star)\cdot\nabla)\boldsymbol{u},\boldsymbol{v})_f^\star + \\ &\quad + \rho_s\left(\tfrac{\boldsymbol{\eta}}{\Delta t^2},\tfrac{\boldsymbol{\psi}}{\Delta t}\right)_s, \\ b(q;\boldsymbol{v})^\star &:= -(q,\nabla\cdot\boldsymbol{v})_f^\star, \end{aligned} \tag{2.4}$$

where $(\boldsymbol{v},\boldsymbol{w})_f^\star := \int_{\Omega_f^\star} \boldsymbol{v}\cdot\boldsymbol{w}\,d\boldsymbol{x}$ and $(\boldsymbol{\psi},\boldsymbol{\chi})_s := \int_{\Omega_s} \boldsymbol{\psi}\cdot\boldsymbol{\chi}\,d\boldsymbol{x}$. Given $\boldsymbol{g} \in \boldsymbol{H}^{1/2}(\Sigma^\star)$, let $\boldsymbol{R}_f(\boldsymbol{g}) \in \boldsymbol{H}^{div}(\Omega_f^\star) := \{\boldsymbol{v} \in \boldsymbol{H}^1(\Omega_f^\star) : \nabla\cdot\boldsymbol{v} = 0\}$ and $\boldsymbol{R}_s(\boldsymbol{g}) \in \boldsymbol{H}^1(\Omega_s)$ be two lifting functions for the FS inteface continuity, defined as

$$\boldsymbol{R}_f(\boldsymbol{g}) - \boldsymbol{R}_s(\boldsymbol{g}) = -\frac{\boldsymbol{g}}{\Delta t} \quad \text{on } \Sigma^\star.$$

Due to the arbitrariness of one of these functions, in what follows we set $\boldsymbol{R}_s(\boldsymbol{g}) = \boldsymbol{0}$. When applied to function $\boldsymbol{\eta}^{m-1}$, we will set $\boldsymbol{R}_f^m := \boldsymbol{R}_f(\boldsymbol{\eta}^{m-1})$.

Then, at each time t^n, the weak formulation of the time discrete semi-implicit forward problem related to (2.1) and (2.2) consists of the following steps. Here, we assume E to be a given function in $\mathcal{E}_{ad}$, and we still denote with $\boldsymbol{u}$ the velocity after the lifting.

1. Compute suitable extrapolations $\Omega_f^\star$, $\boldsymbol{u}^\star$ and $\boldsymbol{w}^\star$ for the approximation of Ω_f^{n+1}, $\boldsymbol{u}^{n+1}$ and $\boldsymbol{w}^{n+1}$.
2. Given $\boldsymbol{f}_f^{n+1} \in \boldsymbol{L}^2(\Omega_f^\star)$ and $\boldsymbol{f}_s^{n+1} \in \boldsymbol{L}^2(\Omega_s)$, find $(\boldsymbol{u}^{n+1},\boldsymbol{\eta}^{n+1}) \in \boldsymbol{Z}^\star$ and $p^{n+1} \in Q^\star$ such that

$$\begin{cases} a(\boldsymbol{u}^{n+1},\boldsymbol{\eta}^{n+1};\boldsymbol{v},\boldsymbol{\psi})^\star + \left(E\,\boldsymbol{S}_s(\boldsymbol{\eta}^{n+1}),\tfrac{1}{\Delta t}\nabla\boldsymbol{\psi}\right)_s + b(p^{n+1};\boldsymbol{v})^\star = \\ \qquad = F_f^{n+1}(\boldsymbol{v}) + F_s^{n+1}\left(\tfrac{\boldsymbol{\psi}}{\Delta t}\right) - a(\boldsymbol{R}_f^{n+1},\boldsymbol{0};\boldsymbol{v},\boldsymbol{\psi})^\star, \\ b(q;\boldsymbol{u}^{n+1})^\star = 0, \end{cases} \tag{2.5}$$

   for all $(\boldsymbol{v},\boldsymbol{\psi}) \in \boldsymbol{Z}^\star$ and $q \in Q^\star$.
3. Update the fluid domain to obtain Ω_f^{n+1} through (2.2).

Functionals F_f^{n+1} and F_s^{n+1} account for forcing terms, boundary data on $\partial\Omega_f^\star \setminus \Sigma^\star$ and $\partial\Omega_s \setminus \Sigma$ and terms coming from the time discretization.

2.4. Properties of the time discrete fluid-structure interaction problem. Let $\|\cdot\|_{L^p}$ and $\|\cdot\|_{H^1}$ be the usual L^p and H^1 norms computed in $\Omega_f^\star$ or Ω_s (for the norms computed on the FS interface, we denote explicitely the dependence of the space on Σ). Given $(\boldsymbol{v},\boldsymbol{\psi}) \in \boldsymbol{Z}^\star$, we also define the following norm for the couple $(\boldsymbol{v},\boldsymbol{\psi})$: $\|(\boldsymbol{v},\boldsymbol{\psi})\|_{Z^\star}^2 := \|\boldsymbol{v}\|_{H^1}^2 + \|\boldsymbol{\psi}\|_{H^1}^2$. Moreover, in what follows, C denotes a

positive constant that does not depend on the solution of the FSI problem or on E, but possibly could depend on the data $\boldsymbol{\eta}_{meas}$, $\boldsymbol{w}^\star$, $\boldsymbol{u}^\star$, F_f, F_s, μ, ρ_f, ρ_s, Δt and on the Neumann and Dirichlet data. When we want to stress the dependence of C on the generic parameter ζ we write $C(\zeta)$. From now on we drop the temporal index of the current solution.

We denote $K := \min(\frac{\rho_f}{\Delta t}, \mu) - \frac{1}{2}\|\nabla \cdot \boldsymbol{w}^\star\|_{L^2}$. Notice that $K > 0$ either when a divergence free ALE extension $\boldsymbol{w}^\star$ is adopted or for Δt small enough and viscosity large enough.

PROPOSITION 1. *Under the assumption $K > 0$ and $E \in \mathcal{E}_{ad}$, problem (2.5) admits a unique solution $(\boldsymbol{u}, \boldsymbol{\eta}) \in \boldsymbol{Z}^\star$ and $p \in Q^\star$. Moreover $\boldsymbol{u}$ and $\boldsymbol{\eta}$, are bounded for $E \in \mathcal{E}_{ad}$.*

Proof. Thanks to the Korn's inequality (see e.g. [4]), for $K > 0$ the bilinear form $a(\cdot, \cdot; \cdot, \cdot) + (E\boldsymbol{S}_s(\cdot), \cdot)$ is coercive

$$a(\boldsymbol{v}, \boldsymbol{\psi}; \boldsymbol{v}, \boldsymbol{\psi}) + (E\boldsymbol{S}_s(\boldsymbol{\psi}), \boldsymbol{\psi}) \geq C(E_{min}) \, \|(\boldsymbol{v}, \boldsymbol{\psi})\|^2_{Z^\star}. \tag{2.6}$$

Moreover, an inf-sup condition holds for problem (2.5) (see e.g. [17]), yielding the well posedness of the problem. Moreover, starting from (2.5) and recalling that $\nabla \cdot \boldsymbol{R}_f = 0$, by taking $(\boldsymbol{v}, \boldsymbol{\psi}) = (\boldsymbol{u}, \boldsymbol{\eta})$ we have for all $E \in \mathcal{E}_{ad}$

$$K\|\boldsymbol{u}\|^2_{H^1} + \frac{\rho_s}{\Delta t^3}\|\boldsymbol{\eta}\|^2_{L^2} + \frac{E_{min}}{\Delta t(1+\nu)}\|\nabla\boldsymbol{\eta}\|^2_{L^2} \leq C\|\boldsymbol{u}\|_{H^1} + C\|\boldsymbol{\eta}\|_{L^2}.$$

Hence

$$\|\boldsymbol{u}\|_{H^1} \leq C, \qquad \|\boldsymbol{\eta}\|_{L^2} \leq C, \qquad \|\boldsymbol{\eta}\|_{H^1} \leq C(E_{min}). \tag{2.7}$$

Bound on the pressure follows from the inf-sup condition (see e.g. [19]). ∎

Upon the previous Proposition, we can introduce a map $\boldsymbol{\eta} : \mathcal{E}_{ad} \to \boldsymbol{W}$ defined for all $E \in \mathcal{E}_{ad}$ by $\boldsymbol{\eta}(E) = \boldsymbol{\eta}$, where $\boldsymbol{\eta}$ is the unique solution of (2.5). Therefore, functional $\mathcal{J}_c$ could be thought as a function of E.

The following bound is an immediate consequence of the previous Proposition, thanks to the trace inequality.

$$\|\boldsymbol{\eta}\|_{L^2(\Sigma)} \leq C. \tag{2.8}$$

Finally, from the equality, valid for any $(\boldsymbol{v}, \boldsymbol{\psi}) \in \boldsymbol{Z}^\star$,

$$\left(E\,\boldsymbol{S}_s(\boldsymbol{\eta}), \frac{1}{\Delta t}\nabla\boldsymbol{\psi}\right)_s = F_f(\boldsymbol{v}) + F_s\left(\frac{\boldsymbol{\psi}}{\Delta t}\right) - a(\boldsymbol{u}, \boldsymbol{\eta}; \boldsymbol{v}, \boldsymbol{\psi})^\star - a(\boldsymbol{R}_f, \boldsymbol{0}; \boldsymbol{v}, \boldsymbol{\psi})^\star,$$

it follows that for any $(\boldsymbol{v}, \boldsymbol{\psi}) \in \boldsymbol{Z}^\star$, thanks to $(2.7)_{1,2}$,

$$\left|\left(E\,\boldsymbol{S}_s(\boldsymbol{\eta}), \frac{1}{\Delta t}\nabla\boldsymbol{\psi}\right)_s\right| \leq C\,\|(\boldsymbol{v}, \boldsymbol{\psi})\|_{Z^\star}. \tag{2.9}$$

2.5. Position of the inverse problem and the KKT conditions. Let us consider the functional

$$\mathcal{J} = \int_\Sigma \left(\boldsymbol{\eta}_{meas}(\boldsymbol{x}, \tau_k) - \boldsymbol{\eta}(\boldsymbol{x}, \tau_k)\right)^2 d\sigma.$$

Then, for each $k = 1, 2, \ldots N$ we consider the following problem.

PROBLEM 2. *Given a regularization term $\mathcal{R}$, find $E \in \mathcal{E}_{ad}$ that minimizes the functional*

$$\mathcal{J}^{\mathcal{R}} = \mathcal{J} + \mathcal{R}(E(\cdot, \tau_k)).$$

under the constraint (2.5).

Following Remark 1, a possible regularization term is given by

$$\mathcal{R}(E) = \frac{\xi}{2} \int_{\Omega_s} \left(E(\boldsymbol{x}, \tau_k) - E_{ref}\right)^2 d\boldsymbol{x}. \tag{2.10}$$

In the sequel, if not otherwise specified, we will refer to the unregularized functional $\mathcal{J}$.

For the sake of the numerical solution, we follow the standard Lagrange multiplier approach. We introduce accordingly the Lagrangian functional at time t^{n_k}, obtained by adding to $\mathcal{J}$ the FSI problem (2.5) as a constraint:

$$\mathcal{L}(\boldsymbol{\mathcal{U}}, \mathcal{P}, \boldsymbol{\mathcal{H}}; \boldsymbol{\lambda}_U, \lambda_P, \boldsymbol{\lambda}_H; \mathcal{E}) = \mathcal{J}(\boldsymbol{\mathcal{H}}; \mathcal{E}) + a(\boldsymbol{\mathcal{U}}, \boldsymbol{\mathcal{H}}; \boldsymbol{\lambda}_U, \boldsymbol{\lambda}_H)^\star +$$

$$+ \left(\mathcal{E}\, \boldsymbol{S}_s(\boldsymbol{\mathcal{H}}), \frac{1}{\Delta t} \nabla \boldsymbol{\lambda}_H \right)_s + b(\mathcal{P}; \boldsymbol{\lambda}_U)^\star + b(\lambda_P; \boldsymbol{\mathcal{U}})^\star +$$

$$- F_f(\boldsymbol{\lambda}_U) - F_s\left(\frac{\boldsymbol{\lambda}_H}{\Delta t}\right) + a(\boldsymbol{R}_f, \boldsymbol{0}; \boldsymbol{\lambda}_U, \boldsymbol{\lambda}_H)^\star.$$

We point out that the Lagrangian functional does not depend on the fluid domain position variable, since the latter is assumed to be known as a consequence of the time semi-implicit discretization.

In order to find the corresponding Euler equations, we impose that in correspondence of the solution $[\boldsymbol{u}, p, \boldsymbol{\eta}; \boldsymbol{\lambda}_u, \lambda_p, \boldsymbol{\lambda}_\eta; E]$ the Gateaux differentials of $\mathcal{L}$ evaluated for any test function vanish. We introduce the following notation. Given N Banach spaces $Z_1, \ldots, Z_N$, let $\boldsymbol{Z} = Z_1 \times Z_2 \times \ldots \times Z_N$ and $\mathcal{M} : \boldsymbol{Z} \to \mathbb{R}$, be such that $(y_1, \ldots, y_N) \in \boldsymbol{Z} \to \mathcal{M}(y_1, \ldots, y_N) \in \mathbb{R}$, and let $< \cdot, \cdot >$ be the duality pairing between $\boldsymbol{Z}'$ and $\boldsymbol{Z}$. We indicate with

$$< d\mathcal{M}_{y_j}[z_1, \ldots, z_N], g >= \lim_{\varepsilon \to 0} \Big(\frac{\mathcal{M}(y_1, .., y_j + \varepsilon g, .., y_N) - \mathcal{M}(y_1, .., y_j, .., y_N)}{\varepsilon} \Big) \Big|_{\boldsymbol{y} = \boldsymbol{z}}$$

the Gateaux differential of $\mathcal{M}$ with respect of y_j, computed at $\boldsymbol{z} = (z_1, \ldots, z_N) \in \boldsymbol{Z}$ and acting along the direction $g \in Z_j$. For the sake of notation, we set $< d\mathcal{M}_{z_j}, g >=< d\mathcal{M}_{y_j}[z_1, \ldots, z_N], g >$.

Then, the solution which minimizes functional $\mathcal{J}$ under the constraint given by the FSI problem is a stationary point of the Lagrangian functional and therefore can be computed by imposing that the gradient of $\mathcal{L}$ vanishes. In particular, by forcing to zero the Gateaux derivatives of the Lagrangian functional with respect to the state variables we formally obtain the *adjoint problem*, namely

$$\begin{cases} < d\mathcal{L}_{\boldsymbol{u}}, \boldsymbol{v} > + < d\mathcal{L}_{\boldsymbol{\eta}}, \frac{\boldsymbol{\psi}}{\Delta t} >= 0 \\ < d\mathcal{L}_p, q >= 0 \end{cases}$$

for all $(\boldsymbol{v}, \boldsymbol{\psi}) \in \boldsymbol{Z}^\star$ and $q \in Q^\star$. The *Optimality condition* is obtained by forcing to zero the explicit derivative with respect to the control variable

$$< d\mathcal{L}_E, \varphi >= 0,$$

for all $\varphi \in L^\infty(\Omega_s)$. These two problems together with the state problem (obtained by vanishing the derivatives of $\mathcal{L}$ with respect to the Lagrange multipliers)

$$\begin{cases} < d\mathcal{L}_{\boldsymbol{\lambda}_u}, \boldsymbol{v} > + < d\mathcal{L}_{\boldsymbol{\lambda}_\eta}, \frac{\boldsymbol{\psi}}{\Delta t} >= 0 \\ < d\mathcal{L}_{\lambda_p}, q >= 0, \end{cases}$$

for all $(\boldsymbol{v}, \boldsymbol{\psi}) \in \boldsymbol{Z}^\star$ and $q \in Q^\star$, yield at each t^{n_k} the following coupled KKT system.

Given $(F_f, F_s) \in (\boldsymbol{Z}^\star)'$ and $\boldsymbol{\eta}_{meas} \in \boldsymbol{W}$, find $E \in \mathcal{E}_{ad}$, $(\boldsymbol{u}, \boldsymbol{\eta}) \in \boldsymbol{Z}^\star, p \in Q^\star, (\boldsymbol{\lambda}_u, \boldsymbol{\lambda}_\eta) \in \boldsymbol{Z}^\star$ and $\lambda_p \in Q^\star$, such that

$$\text{State pbl}: \begin{cases} a(\boldsymbol{u}, \boldsymbol{\eta}; \boldsymbol{v}, \boldsymbol{\psi})^\star + \left(E\, \boldsymbol{S}_s(\boldsymbol{\eta}), \frac{1}{\Delta t} \nabla \boldsymbol{\psi}\right)_s + b(p; \boldsymbol{v})^\star = \\ \qquad\qquad = F_f(\boldsymbol{v}) + F_s\left(\frac{\boldsymbol{\psi}}{\Delta t}\right) - a(\boldsymbol{R}_f, \boldsymbol{0}; \boldsymbol{v}, \boldsymbol{\psi})^\star, \\ b(q; \boldsymbol{u})^\star = 0; \end{cases} \tag{2.11a}$$

$$\text{Adjoint pbl}: \begin{cases} a(\boldsymbol{v}, \boldsymbol{\psi}; \boldsymbol{\lambda}_u, \boldsymbol{\lambda}_\eta)^\star + \left(E\, \boldsymbol{S}_s(\frac{\boldsymbol{\psi}}{\Delta t}), \nabla \boldsymbol{\lambda}_\eta\right)_s + b(\lambda_p; \boldsymbol{v})^\star + \\ \qquad\qquad + \int_\Sigma (\boldsymbol{\eta} - \boldsymbol{\eta}_{meas}) \cdot \boldsymbol{\psi}\, d\sigma = 0, \\ b(q; \boldsymbol{\lambda}_u)^\star = 0; \end{cases} \tag{2.11b}$$

$$\text{Opt. cond}: \quad (\varphi\, \boldsymbol{S}_s(\boldsymbol{\eta}), \nabla \boldsymbol{\lambda}_\eta)_s = 0, \tag{2.11c}$$

for all $(\boldsymbol{v}, \boldsymbol{\psi}) \in \boldsymbol{Z}^\star$, $q \in Q^\star$ and $\varphi \in L^\infty(\Omega_s)$.

The optimality condition states that $\boldsymbol{\eta}$ and $\nabla \boldsymbol{\lambda}_\eta$ have to be orthogonal with respect to the symmetric and coercive operator $\boldsymbol{S}_s$ (this follows by taking $\varphi = 1$ in (2.11c)).

System (2.11) couples two linearized fluid-structure interaction problems and a scalar equation. In particular, for the adjoint problem the interface velocity condition reads

$$\boldsymbol{\lambda}_u = \frac{\hat{\boldsymbol{\lambda}}_\eta}{\Delta t} \quad \text{on } \Sigma^\star,$$

whilst the interface stress condition is

$$\boldsymbol{T}_s(\hat{\boldsymbol{\lambda}}_\eta)\, \boldsymbol{n} - \boldsymbol{T}_f(\boldsymbol{\lambda}_u, \lambda_p)\, \boldsymbol{n} = -\left(\hat{\boldsymbol{\eta}} - \hat{\boldsymbol{\eta}}_{meas}\right), \qquad \text{on } \Sigma^\star. \tag{2.12}$$

The right-hand side takes into account the mismatch between the data and the solution, and modifies the homogeneous interface stress condition $(2.1)_5$ accordingly.

3. Well posedness analysis. Let us start with an existence result. The existence is retrived using the *direct method* in the the calculus of variations. In particular, the basic steps of the proof have been inspired by the work of [26] for the identification of the heat convective term in Robin conditions.

THEOREM 1. *Under the same hypotheses of Proposition 1, for $\xi \geq 0$ there exists at least one minimizer to the optimization Problem 2, with $\mathcal{R}$ defined as in* (2.10).

Proof. Since $\mathcal{J}$ is bounded, $\inf_{E \in \mathcal{E}_{ad}} \mathcal{J}(E) \in \mathbb{R}$ and there exists a sequence $E^k \in \mathcal{E}_{ad}$ such that

$$\lim_{k \to \infty} \mathcal{J}(E^k) = \inf_{E \in \mathcal{E}_{ad}} \mathcal{J}(E).$$

Being E^k bounded in $L^\infty(\Omega_s)$, it follows from the Banach-Alaoglu theorem (see e.g. [44]) that there exists a subsequence of E^k, which we still call E^k, such that

$$E^k \to \bar{E} \quad \text{weakly-* in } L^\infty(\Omega_s),$$

with $\bar{E} \in \mathcal{E}_{ad}$. Let $(\boldsymbol{u}^k, \boldsymbol{\eta}^k) \in \boldsymbol{Z}^\star$ be the solution of (2.11a) associated with E^k. Since bounds on $(\boldsymbol{u}^k, \boldsymbol{\eta}^k) \in \boldsymbol{Z}^\star$ do not depend on E^k, there exists a subsequence $(\boldsymbol{u}^k, \boldsymbol{\eta}^k) \in \boldsymbol{Z}^\star$ weakly converging to $(\bar{\boldsymbol{u}}, \bar{\boldsymbol{\eta}}) \in \boldsymbol{Z}^\star$.

Now, for any $\boldsymbol{\psi} \in \boldsymbol{W}$, it follows that

$$\left(E^k \, \boldsymbol{S}_s(\boldsymbol{\eta}^k), \nabla \boldsymbol{\psi}\right)_s =$$

$$= \left(E^k \left(\boldsymbol{S}_s(\boldsymbol{\eta}^k) - \boldsymbol{S}_s(\bar{\boldsymbol{\eta}})\right), \nabla \boldsymbol{\psi}\right)_s + \left((E^k - \bar{E}) \, \boldsymbol{S}_s(\bar{\boldsymbol{\eta}}), \nabla \boldsymbol{\psi}\right)_s + \left(\bar{E} \, \boldsymbol{S}_s(\bar{\boldsymbol{\eta}}), \nabla \boldsymbol{\psi}\right)_s .$$

The convergence of E^k and $\boldsymbol{\eta}^k$ implies that

$$\lim_{k \to \infty} \left(E^k \, \boldsymbol{S}_s(\boldsymbol{\eta}^k), \nabla \boldsymbol{\psi}\right)_s = \left(\bar{E} \, \boldsymbol{S}_s(\bar{\boldsymbol{\eta}}), \nabla \boldsymbol{\psi}\right)_s . \tag{3.1}$$

Analogously, it can be shown that:

$$\lim_{k \to \infty} a\left(\boldsymbol{u}^k, \boldsymbol{\eta}^k, \boldsymbol{\varphi}, \boldsymbol{\psi}\right) = a\left(\bar{\boldsymbol{u}}, \bar{\boldsymbol{\eta}}, \boldsymbol{\varphi}, \boldsymbol{\psi}\right). \tag{3.2}$$

For construction, $(\boldsymbol{u}^k, \boldsymbol{\eta}^k)$ and E^k satisfy the state equation (2.11a), which reads:

$$\begin{aligned} a(\boldsymbol{u}^k, \boldsymbol{\eta}^k; \boldsymbol{v}, \boldsymbol{\psi})^\star + \left(E^k \boldsymbol{S}_s(\boldsymbol{\eta}^k), \tfrac{1}{\Delta t} \nabla \boldsymbol{\psi}\right)_s + b(p; \boldsymbol{v})^\star = \\ = F_f^{n+1}(\boldsymbol{v}) + F_s^{n+1}\left(\tfrac{\boldsymbol{\psi}}{\Delta t}\right) - a(\boldsymbol{R}_f, \boldsymbol{0}; \boldsymbol{v}, \boldsymbol{\psi})^\star . \end{aligned}$$

Letting k tend to infinity, from equations (3.1) and (3.2), we have that $(\bar{\boldsymbol{u}}, \bar{\boldsymbol{\eta}})$ and $\bar{E}$ satisfies the state equation (2.11a).

We conclude proving that $\bar{E}$ realizes the infimum of J. We recall that, thanks to Rellich-Kondrachov embedding theorem, $\boldsymbol{\eta}^k$ converge strongly to $\bar{\boldsymbol{\eta}}$ in $L^2(\Sigma)$. Moreover, weak$-*$ convergence in L^∞ implies weak convergence in L^2. The weak lower semi-continuity of the functional $\int\limits_{\Omega_s} \left(E^k - E_{ref}\right)^2 d\boldsymbol{x}$ in $L^2(\Omega_s)$ implies that

$$\begin{aligned} &\mathcal{J}(\bar{E}) = \tfrac{1}{2} \int\limits_{\Sigma} \left(\bar{\boldsymbol{\eta}} - \boldsymbol{\eta}_{meas}\right)^2 d\sigma + \tfrac{\xi}{2} \int\limits_{\Omega_s} \left(\bar{E} - E_{ref}\right)^2 d\boldsymbol{x} \leq \\ &\leq \tfrac{1}{2} \lim_{k \to \infty} \int\limits_{\Sigma} \left(\boldsymbol{\eta}(E^k) - \boldsymbol{\eta}_{meas}\right)^2 d\sigma + \tfrac{\xi}{2} \liminf_{k \to \infty} \int\limits_{\Omega_s} \left(E^k - E_{ref}\right)^2 d\boldsymbol{x} \leq \\ &\leq \liminf_{k \to \infty} \left(\tfrac{1}{2} \int\limits_{\Sigma} \left(\boldsymbol{\eta}(E^k) - \boldsymbol{\eta}_{meas}\right)^2 d\sigma + \tfrac{\xi}{2} \int\limits_{\Omega_s} \left(E^k - E_{ref}\right)^2 d\boldsymbol{x} \right) = \\ &= \lim_{k \to \infty} \mathcal{J}(E^k) = \inf_{E \in \mathcal{E}_{ad}} \mathcal{J}(E), \end{aligned}$$

and the thesis is proven. □

Notice that the regularizing term is not strictly needed to the existence theorem.

As we have previosuly pointed out, in practice the displacement retrieved by images and registration is affected by noise (in the image acquisition) and numerical errors (in the registration). For this reason, it is worth investigating the continuous dependence of the minimum $\bar{E}$ on the measurments. Following [26], we have the following result.

PROPOSITION 2. *Let $\boldsymbol{\eta}^k_{meas}$ be a sequence converging to $\boldsymbol{\eta}_{meas}$ in $L^2(\Sigma)$, and E^k a minimizer associated to $\boldsymbol{\eta}^k_{meas}$ as for the previous Proposition. The sequence E^k features a subsequence weak-* converging in $L^\infty(\Sigma)$ to a minimizer of Problem 2.*

Proof. By definition of E^k, we have for all $E \in \mathcal{E}_{ad}$

$$\frac{1}{2} \int_{\Sigma} \left(\boldsymbol{\eta}(E^k) - \boldsymbol{\eta}^k_{meas}\right)^2 d\sigma + \frac{\xi}{2} \int_{\Omega_s} |E^k - E_{ref}|^2 \, d\boldsymbol{x} \leq$$

$$\leq \frac{1}{2}\int_\Sigma \left(\boldsymbol{\eta}(E)-\boldsymbol{\eta}^k_{meas}\right)^2\,d\sigma+\frac{\xi}{2}\int_{\Omega_s}|E-E_{ref}|^2\,d\boldsymbol{x}.$$

By setting again $\bar{E}$ the limit of the bounded sequence E^k, from the latter inequality and the convergence results obtained in the previous Theorem, it follows

$$\mathcal{J}(\bar{E})=\frac{1}{2}\int_\Sigma \left(\boldsymbol{\eta}(\bar{E})-\boldsymbol{\eta}_{meas}\right)^2\,d\sigma+\frac{\xi}{2}\int_{\Omega_s}|\bar{E}-E_{ref}|^2\,d\boldsymbol{x}\leq$$

$$\leq \frac{1}{2}\lim_{k\to\infty}\int_\Sigma \left(\boldsymbol{\eta}(E^k)-\boldsymbol{\eta}^k_{meas}\right)^2\,d\sigma+\frac{\xi}{2}\liminf_{k\to\infty}\int_{\Omega_s}|E^k-E_{ref}|^2\,d\boldsymbol{x}\leq$$

$$\leq \liminf_{k\to\infty}\left(\frac{1}{2}\int_\Sigma \left(\boldsymbol{\eta}(E)-\boldsymbol{\eta}^k_{meas}\right)^2\,d\sigma+\frac{\xi}{2}\int_{\Omega_s}|E-E_{ref}|^2\,d\boldsymbol{x}\right)=\mathcal{J}(E),$$

which proves that $\bar{E}$ is a minimizer of $\mathcal{J}$ for $\|\boldsymbol{\eta}^k_{meas}-\boldsymbol{\eta}_{meas}\|_{L^2(\Sigma)}\to 0$. □

3.1. Properties of $\mathcal{J}$.

PROPOSITION 3. *The following inequality holds*

$$\|\boldsymbol{\eta}_1-\boldsymbol{\eta}_2\|_{L^2(\Sigma)}\leq C(E_{min})\,\|E_2-E_1\|_{L^\infty},\qquad \forall E_1,E_2\in\mathcal{E}_{ad}. \tag{3.3}$$

Since functional $\mathcal{J}$ depends continuously on $\boldsymbol{\eta}$, then it depends continuously on E in the L^∞ topology.

Proof. Let $(\boldsymbol{u}_1,p_1,\boldsymbol{\eta}_1)$ and $(\boldsymbol{u}_2,p_2,\boldsymbol{\eta}_2)$ be the solutions to the equation (2.5) for $E=E_1$ and $E=E_2$, respectively. By subtracting from the state equation with E_1 the one with E_2 and choosing as test functions $(\boldsymbol{v},\boldsymbol{\psi})=(\boldsymbol{u}_1-\boldsymbol{u}_2,\,\boldsymbol{\eta}_1-\boldsymbol{\eta}_2)$, we obtain

$$a(\boldsymbol{u}_1-\boldsymbol{u}_2,\boldsymbol{\eta}_1-\boldsymbol{\eta}_2;\boldsymbol{u}_1-\boldsymbol{u}_2,\boldsymbol{\eta}_1-\boldsymbol{\eta}_2)^\star+\left(E_1\,\boldsymbol{S}_s(\boldsymbol{\eta}_1),\frac{1}{\Delta t}\nabla(\boldsymbol{\eta}_1-\boldsymbol{\eta}_2)\right)_s+$$

$$-\left(E_2\,\boldsymbol{S}_s(\boldsymbol{\eta}_2),\frac{1}{\Delta t}\nabla(\boldsymbol{\eta}_1-\boldsymbol{\eta}_2)\right)_s=0.$$

By adding and subtracting the term $\left(E_1\,\boldsymbol{S}_s(\boldsymbol{\eta}_2),\frac{1}{\Delta t}\nabla(\boldsymbol{\eta}_1-\boldsymbol{\eta}_2)\right)_s$, we have

$$\begin{aligned}a(\boldsymbol{u}_1-\boldsymbol{u}_2,\boldsymbol{\eta}_1-\boldsymbol{\eta}_2;\boldsymbol{u}_1-\boldsymbol{u}_2,\boldsymbol{\eta}_1-\boldsymbol{\eta}_2)^\star+\left(E_1\,\boldsymbol{S}_s(\boldsymbol{\eta}_1-\boldsymbol{\eta}_2),\tfrac{1}{\Delta t}\nabla(\boldsymbol{\eta}_1-\boldsymbol{\eta}_2)\right)_s=\\ =\left((E_2-E_1)\,\boldsymbol{S}_s(\boldsymbol{\eta}_2),\tfrac{1}{\Delta t}\nabla(\boldsymbol{\eta}_1-\boldsymbol{\eta}_2)\right)_s.\end{aligned}$$

By using the inequality (2.9), with $(\boldsymbol{v},\,\boldsymbol{\psi})=(\boldsymbol{u}_1-\boldsymbol{u}_2,\,\boldsymbol{\eta}_1-\boldsymbol{\eta}_2)$, we obtain

$$\begin{aligned}|\,a(\boldsymbol{u}_1-\boldsymbol{u}_2,\boldsymbol{\eta}_1-\boldsymbol{\eta}_2;\boldsymbol{u}_1-\boldsymbol{u}_2,\boldsymbol{\eta}_1-\boldsymbol{\eta}_2)^\star|+\left(E_1\,\boldsymbol{S}_s(\boldsymbol{\eta}_1-\boldsymbol{\eta}_2),\tfrac{1}{\Delta t}\nabla(\boldsymbol{\eta}_1-\boldsymbol{\eta}_2)\right)_s\leq\\ \leq\left\|\tfrac{E_2-E_1}{E_2}\right\|_{L^\infty}\left|\left(E_2\boldsymbol{S}_s(\boldsymbol{\eta}_2),\tfrac{1}{\Delta t}\nabla(\boldsymbol{\eta}_1-\boldsymbol{\eta}_2)\right)_s\right|\leq\\ \leq\tfrac{C}{E_{min}}\,\|E_2-E_1\|_{L^\infty}\|(\boldsymbol{u}_1-\boldsymbol{u}_2,\boldsymbol{\eta}_1-\boldsymbol{\eta}_2)\|_{Z^\star}.\end{aligned}$$

From the coercivity (2.6), it follows that

$$C(E_{min})\|(\boldsymbol{u}_1-\boldsymbol{u}_2,\boldsymbol{\eta}_1-\boldsymbol{\eta}_2)\|^2_{Z^\star}\leq\frac{C}{E_{min}}\,\|E_2-E_1\|_{L^\infty}\|(\boldsymbol{u}_1-\boldsymbol{u}_2,\boldsymbol{\eta}_1-\boldsymbol{\eta}_2)\|_{Z^\star}.$$

Then, from the follow inequalities, holding for all $(\boldsymbol{v}, \boldsymbol{\psi}) \in \boldsymbol{Z}^\star$,

$$\|(\boldsymbol{v}, \boldsymbol{\psi})\|_{Z^\star} \geq \|\boldsymbol{\psi}\|_{H^1} \geq C\|\boldsymbol{\psi}\|_{L^2(\Sigma)},$$

the thesis follows. □

PROPOSITION 4. *For $E \in \mathcal{E}_{ad}$, $\mathcal{J}$ is Gateaux differentiable.*

Proof. From the adjoint problem (2.11b), by following steps analogous to the ones of Proposition 1 and thanks to (2.8), we obtain

$$K\|\boldsymbol{\lambda}_u\|^2_{H^1} + \frac{\rho_s}{\Delta t^3}\|\boldsymbol{\lambda}_\eta\|^2_{L^2} + \frac{E_{min}}{\Delta t(1+\nu)}\|\nabla\boldsymbol{\lambda}_\eta\|^2_{L^2} \leq C\|\boldsymbol{\eta} - \boldsymbol{\eta}_{meas}\|_{L^2(\Sigma)}\|\boldsymbol{\lambda}_u\|_{H^1},$$

and it follows

$$\|\boldsymbol{\lambda}_u\|_{H^1} \leq C, \qquad \|\boldsymbol{\lambda}_\eta\|_{L^2} \leq C, \qquad \|\boldsymbol{\lambda}_\eta\|_{H^1} \leq C(E_{min}). \tag{3.4}$$

We point out that the total Gateaux derivative of $\mathcal{J}$ with respect to E, along a direction $\varphi \in L^\infty$ is given by (see e. g. [22])

$$\left\langle \frac{d\mathcal{J}}{dE}, \varphi \right\rangle = \langle d\mathcal{L}_E, \varphi \rangle = \frac{1}{\Delta t}\left(\varphi\, \boldsymbol{S}_s(\boldsymbol{\eta}), \nabla\boldsymbol{\lambda}_\eta\right)_s. \tag{3.5}$$

The linear operator $\frac{d\mathcal{J}}{dE}$ is bounded, in fact

$$\left|\left\langle \frac{d\mathcal{J}}{dE}, \varphi \right\rangle\right| \leq C\|\varphi\|_{L^\infty}\, \|\boldsymbol{\eta}\|_{H^1}\|\boldsymbol{\lambda}_\eta\|_{H^1} \tag{3.6}$$

and $\|\boldsymbol{\eta}\|_{H^1}$, $\|\boldsymbol{\lambda}_\eta\|_{H^1}$ are bounded thanks to (2.7) and (3.4). □

For a usual regularizing term $\mathcal{R}$ such as in (2.10), Gateaux differentiability of $\mathcal{J}^\mathcal{R}$ is therefore guaranteed in $E \in \mathcal{E}_{ad}$.

When $J^\mathcal{R}$ has a minimum in $\bar{E}$ belonging to the interior of a set $\mathcal{E}_{ad}$, then the Gateaux derivative of $J^\mathcal{R}$ in any direction must be zero, leading to the KKT system. However, solution $\bar{E}$ can in general belong to $\partial\mathcal{E}_{ad}$. In this case, KKT system is not guaranteed to have a solution. There are however some particular choices of the admissible set $\mathcal{E}_{ad}$, combined with a proper regularizing term, where E belongs to the interior of $\mathcal{E}_{ad}$ and then the solution to KKT system does exist. This will be the topic of the next subsection.

3.2. Special choices of $\mathcal{E}_{ad}$. We consider two cases, $E \in W^{1,\infty}(\Omega_s)$ and E given by a linear combination of suitable functions. In both cases, we will able to prove the existence of (at least) one minimizer in $(0, +\infty)$.

PROPOSITION 5. *Let us consider $\mathcal{E}_{ad} := \{E : E \in W^{1,\infty}(\Omega_s), E > 0\}$, and the regularization term $\mathcal{R}(E) = \frac{\xi}{2}\left\|\log\left(\frac{E}{E_{ref}}\right)^2\right\|_{W^{1,\infty}}$. Then, for $\xi > 0$ there exists at least one minimizer to the optimization Problem 2.*

Proof. Let μ be the infimum of $\mathcal{J}^\mathcal{R}$, namely $\mu = \inf_{E>0}\mathcal{J}^\mathcal{R}$. Let us consider the minimizing sequence $\mathcal{J}^\mathcal{R}(E^k) \to \mu$, $E^k \in \mathcal{E}_{ad}$. Then, there exists $\varepsilon > 0$, such that for k large enough,

$$\mathcal{J}(E^k) + \mathcal{R}(E^k) = \mathcal{J}^\mathcal{R}(E^k) \leq \mu + \varepsilon.$$

Hence, in particular,

$$\mathcal{R}(E^k) = \frac{\xi}{2}\left\|\log\left(\frac{E^k}{E_{ref}}\right)^2\right\|_{W^{1,\infty}} \leq \mu + \varepsilon$$

This inequality implies that E^k belongs to a bounded and closed set $\mathcal{E}$ in $W^{1,\infty}(\Omega_s)$ and moreover we have that

$$E_{ref}\exp\left(-\sqrt{\frac{2(\mu+\varepsilon)}{\xi}}\right) \leq E^k \leq E_{ref}\exp\left(\sqrt{\frac{2(\mu+\varepsilon)}{\xi}}\right).$$

Since the embedding of $W^{1,\infty}$ in L^∞ is compact [13], there exists a subsequence E^k converging to $\bar{E} \in \mathcal{E}$ in the L^∞ topology. The regularization term $\mathcal{R}(E)$ is lower semicontinuous in L^∞. In fact it can be written in the form $\mathcal{R} = \frac{\xi}{2}\|f(u, Du)\|_{L^\infty}$, with $u = \log\left(\frac{E}{E_{ref}}\right)^2$ and f convex with respect to the second argument and the lower semicontinuity of $\mathcal{R}$ follows from the Corollary 1.5 in [21]. Thanks to the continuity of $\mathcal{J}$ (Proposition 3), and the lower semicontinuity of $\mathcal{R}$, we have that $\mathcal{J}^{\mathcal{R}}(\bar{E}) = \inf_{E>0}\mathcal{J}^{\mathcal{R}}$. □

Similarly, we consider the case in which E is given by a linear combination of functions $\varphi_i \in L^\infty(\Omega_s)$, namely $E = \sum_{i=1}^N a_i\,\varphi_i$, with $\boldsymbol{a} = [a_1, \ldots, a_N] \in \mathbb{R}^N$. Precisely, we limit the analysis to a set of functions φ_i which satisfy the following property, for any $E_1, E_2 \in \mathbb{R}^+$ and $\boldsymbol{a} \in \mathbb{R}^N$

$$\sum_{i=1}^N a_i\varphi_i(\boldsymbol{x}) \in [E_1, E_2], \forall \boldsymbol{x} \in \Omega_s \iff \boldsymbol{a} \in [E_1, E_2]^N. \tag{3.7}$$

We point out that piecewise constant and piecewise linear functions fulfill property (3.7).

PROPOSITION 6. *Let us consider the set* $\mathcal{E}_{ad} := \{E : E = \sum_{i=1}^N a_i\,\varphi_i,\ \boldsymbol{a} \in \mathbb{R}^N, a_i > 0, \forall i\}$, *where the functions* $\varphi_i \in L^\infty(\Omega_s)$ *satisfy the property* (3.7). *Let us take* $\mathcal{R}(E) = \frac{\xi}{2}\left\|\log\left(\frac{E}{E_{ref}}\right)\right\|^2_{L^\infty}$. *Then, for* $\xi > 0$ *there exists at least one minimizer to the optimization Problem 2.*

Proof. Let μ be the infimum of $\mathcal{J}^{\mathcal{R}}$, namely $\mu = \inf_{E\in\mathcal{E}}\mathcal{J}^{\mathcal{R}}$. Let us consider the minimizing sequence $\mathcal{J}^{\mathcal{R}}(E^k) \to \mu$, $E^k \in \mathcal{E}_{ad}$. Then, there exists $\varepsilon > 0$, such that for k large enough,

$$\mathcal{J}(E^k) + \mathcal{R}(E^k) = \mathcal{J}^{\mathcal{R}}(E^k) \leq \mu + \varepsilon,$$

Hence

$$\mathcal{R}(E^k) = \frac{\xi}{2}\left\|\log\left(\frac{E^k}{E_{ref}}\right)\right\|^2_{L^\infty} \leq \mu + \varepsilon.$$

The sequence E^k reads $E^k = \sum_{i=1}^N a_i^k\,\varphi_i$. Hence the above inequlity, together with property (3.7), implies that the sequence $\boldsymbol{a}^k$ belongs to the compact set $[E_1, E_2]^N$, with $E_1 = E_{ref}\exp\left(-\sqrt{\frac{2(\mu+\varepsilon)}{\xi}}\right)$ and $E_2 = E_{ref}\exp\left(\sqrt{\frac{2(\mu+\varepsilon)}{\xi}}\right)$. It is therefore possible to extract two subequences, such that $\boldsymbol{a}^k \to \bar{\boldsymbol{a}} \in [E_1, E_2]^N$. Hence $E^k \to \bar{E} := \sum_{i=1}^N \bar{a}_i\varphi_i$. Thanks to the continuity of $\mathcal{J}$ (Proposition 3) and of $\mathcal{R}$ in $L^\infty(\Omega_s)$ we have that $\mathcal{J}^{\mathcal{R}}(\bar{E}) = \inf_{E>0}\mathcal{J}^{\mathcal{R}}$. □

4. Numerical solution of the IFSI problem. In order to solve the nonlinear minimization problem, we choose to eliminate the dependence of $\mathcal{J}^{\mathcal{R}}$ on the state variables $(\boldsymbol{u}, \boldsymbol{\eta})$, by solving the state equation. In this way we can use standard

solvers for the state equations and standard optimization tools for minimizing $\mathcal{J}^{\mathcal{R}}$. In particular we are willing to use gradient-based methods such as the *steepest descent* method and the *Broyden-Fletcher-Goldfarb-Shanno* (BFGS) method (see e. g. [32]). This is a common choice when solving PDE-constraint optimization problems, since the gradient of the functional can be effectively computed using the adjoint equation (see, e. g., [22]). Gradient-based methods require to evaluate the functional $\mathcal{J}^{\mathcal{R}}(E^k)$ and/or the functional derivative $\frac{d\mathcal{J}^{\mathcal{R}}}{dE}\Big|_{E^k}$ for some value of the control variable E^k. We solve first the state equation to get $\boldsymbol{\eta}^k$ and then we evaluate $\mathcal{J}^{\mathcal{R}}(E^k) = \mathcal{J}(\boldsymbol{\eta}^k(E^k)) + \mathcal{R}(E^k)$. Moreover, once $\boldsymbol{\lambda}_\eta^k$ is obtained by solving the adjoint equation, from (3.5) it follows that the derivative can be computed with the following expression

$$\left\langle \frac{d\mathcal{J}^{\mathcal{R}}}{dE}\Big|_{E^k}, \varphi \right\rangle = \frac{1}{\Delta t}\left(\varphi\, \boldsymbol{S}_s(\boldsymbol{\eta}^k), \nabla\boldsymbol{\lambda}_\eta^k\right)_s + \left\langle \frac{d\mathcal{R}}{dE}\Big|_{E^k}, \varphi \right\rangle.$$

REMARK 3. *BFGS is a method devised for unconstrained optimization, while the problem at hand features the constrain $E > 0$. To overcome this problem, we use as a control variable $\psi = \log(E)$, so that $E = \exp(\psi) > 0$ for every $\psi \in L^\infty(\Omega_s)$. We notice that $\frac{d\mathcal{J}^{\mathcal{R}}}{d\psi}\Big|_{\psi^k}$ is given then by*

$$\left\langle \frac{d\mathcal{J}^{\mathcal{R}}}{d\psi}\Big|_{\psi^k}, \varphi \right\rangle = \frac{1}{\Delta t}\left(\varphi E^k\, \boldsymbol{S}_s(\boldsymbol{\eta}^k), \nabla\boldsymbol{\lambda}_\eta^k\right)_s + \left\langle \frac{d\mathcal{R}}{d\psi}\Big|_{\psi^k}, \varphi \right\rangle, \qquad \forall \varphi \in L^\infty(\Omega_s).$$

4.1. Finite Element Discretization. Let $\boldsymbol{Z}_h$ be a finite dimensional subspace of $\boldsymbol{Z}$, Q_h a finite dimensional subspace for the pressure and E_h the finite dimensional subspace for E. In particular we will refer basically to a Lagrange finite element approximation of the problem and we denote with N the total degrees of freedom of the FSI problem.

For the state and the adjoint problems, we introduce the vector of the unknowns $\boldsymbol{U} \in \mathbb{R}^N$ and $\boldsymbol{\Lambda}_U \in \mathbb{R}^N$, respectively, whose entries collect all the unknown of velocity, pressure and displacement and the corresponding Lagrange multipliers. For easiness of implementation we introduce a measurements vector $\boldsymbol{U}_{meas} \in \mathbb{R}^N$. The only entries of $\boldsymbol{U}_{meas}$ actually used are the ones corresponding to the structure interface degrees of freedom.

We introduce the FSI finite-element matrix $A \in \mathbb{R}^{N\times N}$ related to the bilinear forms $a(\cdot,\cdot;\cdot,\cdot)$ and $b(\cdot;\cdot)$ defined in (2.4) (the latter being extended with zero entries in the structure degrees of freedom) and the finite-element matrices $K \in \mathbb{R}^{N\times N}$ and $K_S \in \mathbb{R}^{N\times N}$ associated with the bilinear forms $\left(E\boldsymbol{S}_s(\cdot), \frac{1}{\Delta t}\nabla\cdot\right)_s$ and $\left(\boldsymbol{S}_s(\cdot), \frac{1}{\Delta t}\nabla\cdot\right)_s$ (extended with zero entries in the fluid degrees of freedom). Moreover, we set

$$(M_\Sigma)_{kl} := \int_{\Sigma^\star} \boldsymbol{\zeta}_k \cdot \boldsymbol{\zeta}_l \, d\sigma, \quad k,l = 1,\dots,N,$$

where the $\boldsymbol{\zeta}_l$ are the structure basis functions related to the mesh interface nodes $\boldsymbol{x}_j$, $j = 1,\dots,N_{interf}$ for the structure displacement degrees of freedom, whilst are the zero functions for the fluid velocity and pressure degrees of freedom.

We assume that measures are available in all the nodes of the finite element mesh. This can be assumed to be realistic after a proper interpolation of the map retrieved by the registration procedure. A careful analysis of the impact of the interpolation

error on the accuracy of the compliance estimation is beyond the scope of the present work and will be investigated elsewhere.

The algebraic counterpart of system (2.11) reads

$$\begin{cases} (A + K(\boldsymbol{E}))\,\boldsymbol{U} = \boldsymbol{F}, \\ M_\Sigma\,\boldsymbol{U} + (A^T + K^T(\boldsymbol{E}))\,\boldsymbol{\Lambda}_U = \boldsymbol{F}_\Lambda + M_\Sigma\,\boldsymbol{U}_{meas}, \\ \boldsymbol{U}^T K_S\,\boldsymbol{\Lambda}_U = 0, \end{cases} \tag{4.1}$$

for suitable vectors $\boldsymbol{F}$ and $\boldsymbol{F}_\Lambda$.

We detail the algorithm to solve the non-linear system (4.1), in the case the steepest descent method is used and $\xi = 0$ (no regularization term).

ALGORITHM 1. *For $k = 1, \ldots$ up to the fulfilment of a given convergence test:*

1. *Solve the linear system*

$$(A + K(\boldsymbol{E}_k))\boldsymbol{U}_k = \boldsymbol{F};$$

2. *Solve the linear system*

$$(A^T + K^T(\boldsymbol{E}_k))(\boldsymbol{\Lambda_U})_k = \boldsymbol{F}_\Lambda - M_\Sigma(\boldsymbol{U}_k - \boldsymbol{U}_{meas});$$

3. *Given a suitable $\delta_k \in \mathbb{R}$, update*

$$\boldsymbol{E}_{k+1} - \boldsymbol{E}_k = \delta_k\,\boldsymbol{U}_k^T\,K_S\,(\boldsymbol{\Lambda}_U)_k;$$

4. *Stopping criterion: condition on the gradient of $\mathcal{J}$*

$$\|\boldsymbol{U}_k^T\,K_S\,(\boldsymbol{\Lambda}_U)_k\| \leq \varepsilon.$$

Since for the BFGS scheme we have used the Gnu Scientific Library [18] (see Section 6.1), we do not detail this scheme in what follows and we refer the reader to [32]. We remark that we have used the same stopping criterion as in Algorithm 1.

5. Numerical results. In this Section we assume that the Young modulus E is constant in space, which is reasonable for healthy vessels over small regions.

As we have pointed out in the Introduction, the numerical results presented here do not rely upon a real image registration, but on synthetic data, with the purpose of assessing the accuracy and the reliability of the method. The problem is therefore formulated over 2D domains (for both the fluid and the structure). The displacement data $\boldsymbol{\eta}_{meas}$ are generated by the solution $\boldsymbol{\eta}_{fwd}$ over $\Sigma^\star$ of the forward problem for a given value of the Young modulus, taken within a physiological range. The knowledge of the "exact" Young modulus allows a quantitative analysis of the accuracy and the robustness of the method. We consider at first simple rectangular domain mimicking a 2D pipe. We analyze the impact of (artificially added) noise to the synthetic data and of different sampling frequencies of the displacement. More precisely, in the instants when the displacement measures are available the IFSI problem is solved. In the other instants of the time discretization, the usual forward FSI problem is solved using the last Young modulus estimate available. The latter is used as initial guess for the successive IFSI problem to be solved. Successively, we consider a more realistic domain, mimicking a 2D arterial bifurcation.

For the 2D structure we consider the following equation of linear elasticity (see e.g. [37, 42])

$$\rho_s \partial_{tt}\boldsymbol{\eta} - \gamma_1 \nabla \cdot (\nabla\boldsymbol{\eta} + (\nabla\boldsymbol{\eta})^t) - \gamma_2 \nabla \cdot ((\nabla \cdot \boldsymbol{\eta})\boldsymbol{I}) + \beta\boldsymbol{\eta} = \boldsymbol{0},$$

where $\beta = E/((1-\nu^2)R^2)$ and R is the radial dimension of the fluid domain. The latter term accounts transversal membrane effects in the 2D domain (see [42]). This term does not affect the analysis carried out in the previous Sections, that is readily extended. For the fluid, we assign the following impulsive Neumann condition at the inlet

$$p\boldsymbol{n} - \mu\left(\nabla\boldsymbol{u} + \nabla\boldsymbol{u}^T\right)\cdot\boldsymbol{n} = P(t)\boldsymbol{n}$$

where

$$P(t) = \begin{cases} 2\cdot 10^4\, dyne/cm^2 & t \le 0.005\, s, \\ 0 & t > 0.005\, s. \end{cases}$$

Homogeneous Neumann condition is prescribed at the outlets. In a real context these conditions need to be replaced by *in vivo* measurements on either blood velocity or pressure.

In all the simulations of the present Section we set $\rho_f = 1\, g/cm^2$, $\rho_s = 1.1\, g/cm^2$, $\mu = 0.035\, Poise$, $h = 0.02\, cm$ and $\Delta t = 0.001\, s$. We use a `Matlab` Finite Element code where Algorithm 1 is implemented, with a tolerance $\varepsilon = 10^{-6}$, and we use P1bubble-P1 finite elements spaces for the fluid subproblem and P1 elements for the structure subproblem.

Moreover, we do not consider any regularization term in the functional ($\xi = 0$). The FSI state and adjoint problems are solved with a monolithical approach.

5.1. Results in a 2D pipe. In this section, we consider the domains $\Omega_f^0 = (0, 6s)\times(0,1)$ and $\Omega_s = ((0,6)\times(0.5,0.6))\cup((0,6)\times(-0.6,-0.5))$, where the inlet is given by $\Gamma_{in} := \{0\}\times(0,1)$. To obtain the data, we consider the constant (realistic) value $E_{data} = 1.3\cdot 10^6\, dyne/cm^2$ for the forward simulation. Moreover, we set $\nu = 0.3$.

In the first set of simulations we assume that displacement field $\boldsymbol{\eta}_{meas}$ is available in each grid point of the space discretization and in each instant of the time discretization. In Figure 5.1 we show the convergence history of the control variable E_k at the first time step, starting from different values of the initial Young modulus E_0. In this case we use the value $\delta_k = 110\, E_k$, empirically tuned. In all the three

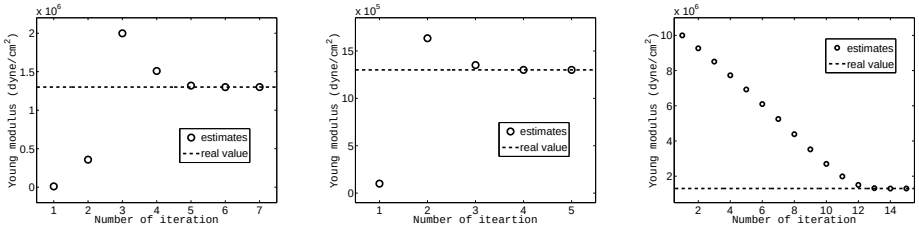

FIG. 5.1. *Convergence history of E_k at the first time step for different values of the initial guess of Young modulus: $E_0 = 10^4\, dyne/cm^2$ (left), $E_0 = 10^5\, dyne/cm^2$ (middle), $E_0 = 10^7\, dyne/cm^2$ (right). With the horizontal line we have depicted the value E_{data}.*

cases the convergence is achieved within a few iterations. For the subsequent time steps, convergence is invariably obtained in just 1 iteration. This is not surprising since the data are not affected by any noise.

In Figure 5.2 we report the wall-normal displacement obtained with the "forward" simulation ("data") and computed by solving the IFSI problem, by choosing $E_0 = 10^5\, dyne/cm^2$ as initial guess at the first time step.

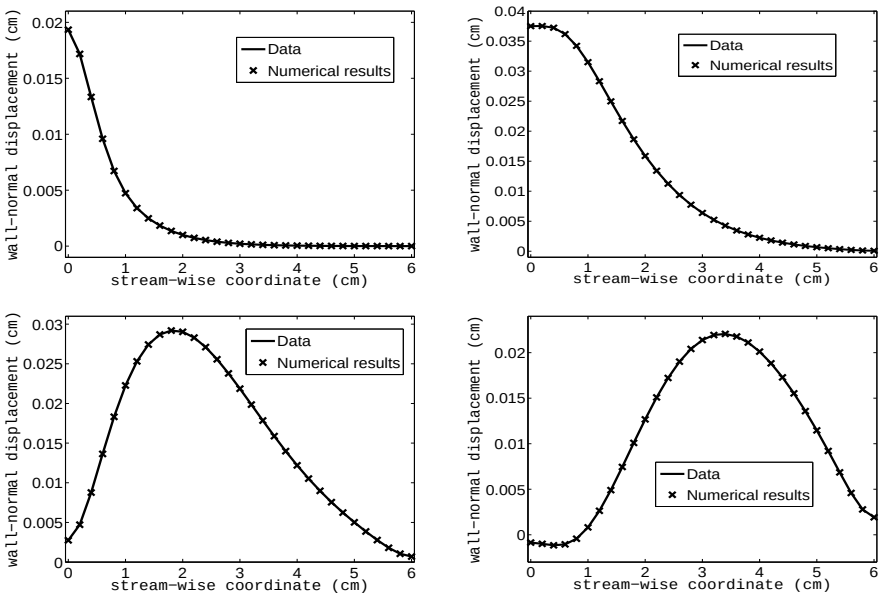

FIG. 5.2. *Data obtained by the "forward" numerical simulation (solid line) and wall-normal displacement obtained with the proposed methodology. Time:* $t = 0.001\,s$ *(up, left),* $t = 0.004\,s$ *(up, right),* $t = 0.007\,s$ *(bottom, left),* $t = 0.010\,s$ *(bottom, right).*

Impact of noise. In the second set of simulations, we add to the data obtained by the forward simulation a random space-dependent noise in order to mimick the measurement error of the acquisition/registration procedure. Again, we assume displacements data available at all the instants of the time discretization.

In particular, at each time step we add a uniform noise $\boldsymbol{\nu}_P$ to the data coming from the forward simulations ($\boldsymbol{\eta}_{meas} = \boldsymbol{\eta}_{fwd} + \boldsymbol{\nu}_P$). Precisely we take $\boldsymbol{\nu}_P = P\,M\,\boldsymbol{\mathcal{U}}(-0.5, 0.5)$, where P is a percentage of error, M the maximum in space of the absolute value of displacement obtained by the forward simulation, and $\boldsymbol{\mathcal{U}}$ the (vector) uniform probability distribution in the interval $[-0.5, 0.5]$. In Figure 5.3 we show the noisy data obtained with $P = 0.1$ compared with the original signal and with the results of the numerical simulation after the optimization process. In this case,

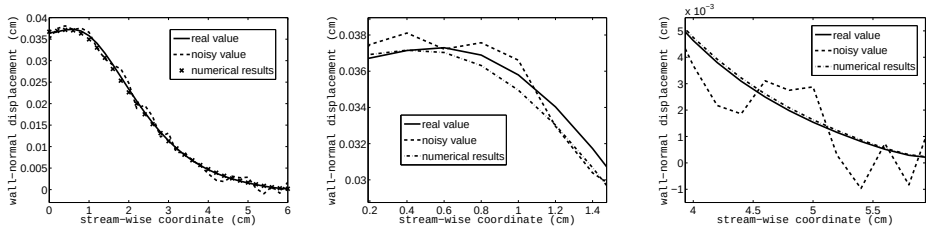

FIG. 5.3. *Data obtained with the "forward" numerical simulation without and with noise (*$P = 0.1$*), and wall-normal displacement obtained by the numerical simulation. Time:* $t = 0.005\,s$.

the converged values of the Young modulus at each time step are different, since the data are affected by a time-dependent error. Since we have assumed E to be constant in time, a simple way for filtering the effect of noise is to average the sequence of

estimates for E^k, $k = 1, \ldots$. We perform the average over 10 steps. In Table 5.1 we report the mean estimated Young modulus and the standard deviation over 5 simulations corresponding to 5 different realizations of the noise, for different values of noise percentage P and initial guesses E_0. The results show small standard deviation in all the cases, suggesting that the simple average in this case is enough for filtering the inaccuracies induced by the noise. In Table 5.1 we report the mean of the percentage errors and of the number of iterations needed to reach convergence.

$\downarrow E_0 \setminus P \rightarrow$	1%	5%	10%
$10^4\, dyne/cm^2$	1.2799 ± 0.0027	1.2565 ± 0.0255	1.2253 ± 0.0134
	1.54% (1.3)	3.34% (1.2)	5.74% (1.2)
$10^5\, dyne/cm^2$	1.2803 ± 0.0041	1.2717 ± 0.0090	1.2802 ± 0.0526
	1.52% (1.1)	2.18% (1.1)	3.39% (1.1)
$10^7\, dyne/cm^2$	1.3147 ± 0.0180	1.3565 ± 0.0248	1.3424 ± 0.0299
	1.63% (2.3)	4.43% (2.2)	3.36% (2.2)

TABLE 5.1

Random noise case. Mean and standard deviation of the five estimates (to be multiplied by 10^6, top) and mean percentage error and number of iterations (bottom) for different values of the initial guess of the Young modulus and of the percentage of random noise.

A remarkable and pretty unexpected feature of these results is that even in presence of large noise mean error is below 6%.

Data under-sampling (sparse data). In the third set of simulations, we suppose to know the measured data $\boldsymbol{\eta}_{meas}$ only at a particular subset of interface nodes and time discretization instants (*sparse data*). In particular, if $\boldsymbol{x}_k$ are the interface nodes, we use the acquired data at points $\boldsymbol{x}_k^{meas} = \boldsymbol{x}_{pk}$, $p \in \mathbb{N}$, and at instants $n_i = q\, i$, $q \in \mathbb{N}$, and set $E_0 = 10^6\, dyne/cm^2$. In Table 5.2 we report the mean percentage error and the mean number of iterations (in brackets) obtained by running 5 simulations with different random noise and over 10 time steps. In the instants when the displacements field $\boldsymbol{\eta}_{meas}$ is not available, we simply solve the forward FSI problem with the current guess for the Young modulus. Alternatively, an interpolation of the available data over all (or a part of) the time steps could be considered.

We observe that by decreasing the number of informations used in the minimization procedure, both the error and the number of iterations increases. A more detailed

$P \rightarrow$	1%	5%
$p = 2,\ q = 1$	3.4% (1.3)	2.9% (2.4)
$p = 4,\ q = 1$	6.9% (4.8)	6.7% (6.9)
$p = 2,\ q = 2$	5.2% (1.7)	4.4% (3.5)
$p = 4,\ q = 2$	8.6% (4.5)	7.7% (9.4)

TABLE 5.2

Spot data case. Mean percentage error and number of iterations (in brackets) for different values of the percentage of random noise, and of values of p and q.

quantitative analysis aiming at showing which is the minimal number of informations needed to have a robust estimate of E is under investigation.

5.2. 2D arterial bifurcation. In this section we present the results obtained by applying the proposed methodology to a 2D geometry of a simplified arterial

bifurcation. In this case we set $\nu = 0.49$ in order to take into account the quasi-incompressibility of the human arteries, and $E_{data} = 3.5 \cdot 10^6\, dyne/cm^2$. In Fig. 5.4,

$2.5 \cdot 10^5\, dyne/cm^2$	$3.499991\, dyne/cm^2$
	0.00025% (2.25)
$2.5 \cdot 10^6\, dyne/cm^2$	$3.500017\, dyne/cm^2$
	0.00049% (2.87)
$2.5 \cdot 10^7\, dyne/cm^2$	$3.499982\, dyne/cm^2$
	0.00051% (4.37)

TABLE 5.3

Carotid simulation. Average of the converged estimates of the Young modulus (to be multiplied by 10^6) over 8 time steps (up), percentage error (bottom) and mean number of iterations to reach coonvergence (bottom, in brachets).

on the left, the pressure in the deformed fluid domain and the exploded position of the structure obtained with the forward simulation are shown at 3 different instants. On the right of the same figure, the differences of pressure solutions obtained with the forward simulation and with the proposed methodology (with $E_0 = 2.5 \cdot 10^5\, dyne/cm^2$) are plotted in the reference domain. In Table 5.3, we show the values of the average of the converged Young modulus over 8 time steps, the percentage error and the mean number of iterations needed to reach convergence. We point out that Algorithm 1 both in term of accuracy and in terms of convergence performs in a remarkably efficient way.

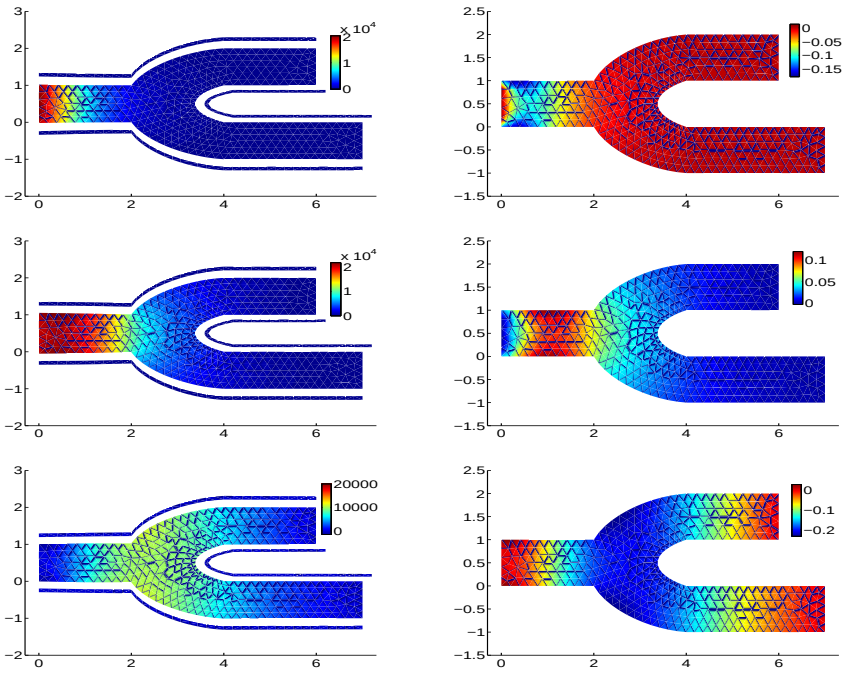

FIG. 5.4. *Carotid simulation. Results obtained with the "forward" numerical simulation (left) and differences with the solution obtained with the proposed methodology (right). Time: $t = 0.002\, s$ (up), $t = 0.005\, s$ (middle), $t = 0.008\, s$ (bottom), $t = 0.010\, s$.*

6. The membrane structure model. As pointed out previously, with current devices displacement is mainly retrieved on the interface between fluid and structure. The thickness of a vascular wall on the other hand is usually thinner than the dimension of the lumen. In order to reduce the computational time, we could consider the vascular wall as a thin membrane more than as a full "thick" structure.

6.1. Problem setting. A simplified membrane model for the normal displacement $\eta := \boldsymbol{\eta} \cdot \boldsymbol{n}$ has been proposed in [37, 31], namely

$$\rho_s \partial_{tt}\eta + E\,\beta\,\eta = 0, \qquad \text{in } \Sigma,$$

with

$$\beta = \frac{h_s}{1-\nu^2}(4\rho_1^2 - 2(1-\nu)\rho_2),$$

where ρ_1 and ρ_2 are respectively the *mean curvature* and the *Gaussian curvature*, and h_s is the thickness of the membrane. Moreover, in [31] it has been also showed that after time discretization, the FSI problem can be reduced to a purely fluid problem with Robin boundary conditions at the fluid structure interface.

Let us define $\boldsymbol{V}_m^\star$ and $\mathcal{E}_m^{ad}$ as:

$$\boldsymbol{V}_m^\star := \{\boldsymbol{v} \in \boldsymbol{V}^\star : (\boldsymbol{v} - (\boldsymbol{v}\cdot\boldsymbol{n})\boldsymbol{n})|_{\Sigma^\star} = \boldsymbol{0}\},\ \mathcal{E}_m^{ad} := \{E \in L^\infty(\Sigma) : 0 < E_{min} \le E \le E_{max}\}.$$

Then, the fluid-membrane interaction problem reads:
Given η^{n-1} and η^{n-2} in $H^{1/2}(\Sigma)$ and $\boldsymbol{u}^n \in \boldsymbol{V}_m^n$, find $\boldsymbol{u} \in \boldsymbol{V}_m^\star$, $p \in Q^\star$, $\eta \in H^{1/2}(\Sigma)$ and $E \in \mathcal{E}_m^{ad}$ such that

$$\begin{cases} \dfrac{\rho_f}{\Delta t}\,(\boldsymbol{u} - \boldsymbol{u}^n, \boldsymbol{v})_f^\star + (\boldsymbol{T}_f(\boldsymbol{u}, p), \nabla \boldsymbol{v})_f^\star + \rho_f\,((\boldsymbol{u}^\star - \boldsymbol{w}^\star)\cdot\nabla)\boldsymbol{u}, \boldsymbol{v})_f^\star + b(p, \boldsymbol{v}) + \\ \qquad + \displaystyle\int_{\Sigma^\star} \left(\frac{\rho_s h_s}{\Delta t} + E\beta\Delta t\right) \boldsymbol{u}\cdot\boldsymbol{n}\,\boldsymbol{v}\cdot\boldsymbol{n}\,d\sigma + \\ \qquad - \displaystyle\int_{\Sigma^\star} \left(\frac{\rho_s h_s}{\Delta t^2}\left(\hat\eta^n - \hat\eta^{n-1}\right) - E\beta\,\hat\eta^n\right) \boldsymbol{v}\cdot\boldsymbol{n}\,d\sigma = 0, \\ b\,(q, \boldsymbol{u}) = 0, \\ \hat\eta = \hat\eta^n + \Delta t(\boldsymbol{u}\cdot\boldsymbol{n}|_{\Sigma^\star}), \end{cases} \tag{6.1}$$

for all $\boldsymbol{v} \in \boldsymbol{V}_m^\star$ and $q \in Q^\star$. In this case, the functional to be minimized reads

$$\mathcal{J}_m(E) = \frac{1}{2}\int_\Sigma (\eta(E) - \boldsymbol{n}\cdot\boldsymbol{\eta}_{meas})^2\,d\sigma.$$

As in the case of the thick structure, we find the necessary conditions for E by solving the KKT system.

Since $\beta \ge 0$, under the same hypotheses of Proposition 1 it is possible to prove that there exists a unique solution to problem (6.1). Moreover $\boldsymbol{u}$ is bounded in $\boldsymbol{H}^1(\Omega_f^\star)$ (see [31]). Therefore, Theorem 1 and Propositions 5 and 6 extend straightforwardly.

6.2. Numerical results. In this section we present two test cases. In the first one we consider an axisymmetric tube whose wall has a constant Young modulus. In the second one we consider a simplified axisymmetric geometry representing an abdominal aneurysm with a piecewise linear Young modulus for the aneurysm wall.

In the following simulations, we use as the control variable $\psi = \log(E)$. With abuse of notation, the functional is $\mathcal{J}(\psi) := \mathcal{J}(E(\psi)) = \mathcal{J}(\exp(\psi))$. To find a

minimum of $\mathcal{J}$, we resort to the BFGS method provided by the Gnu Scientific Library [18]. As tolerance in the stopping criterion we use $\varepsilon = 1e-3$. Moreover, if not otherwise specified, we do not consider any regularization term in the functional.

We use the Finite Element Library `LIFEV` implemented in C++ (`www.lifev.org`), with the same parameters and Finite Elements used in Section 5.

6.2.1. Numerical results on an axisymmetric tube. In these simulations, we solve the problem in a cylinder of radius $R = 0.5\ cm$ and height $H = 6\ cm$, which may represent an artery. We impose the pressure drop $\Delta p = 10^4\, dyne/cm^2$ for the first 5 ms between the inlet and the outlet of the vessel. As before, we solve a forward problem with $E = 1.3e6\ dyne/cm^2$, obtaining the displacement η_{fwd} over Σ as the data for the control problem. Figure 6.1 shows the geometry and the pressure along a section of the cylinder, for different time instants.

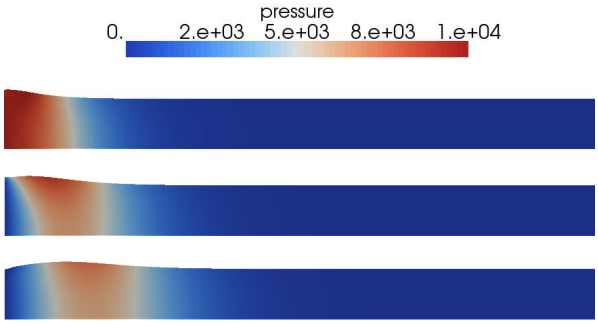

FIG. 6.1. *2d axisymmetric simulation. Geometry at time $t = 4\ ms$, $t = 6\ ms$ and $t = 8\ ms$. Coloured with blood pressure.*

We solve the optimization problem over the first 10 time steps, corresponding to the first 10 ms of the simulation. The most of the computational cost is due to the solutions of the state and adjoint equations, which in this case are purely fluid problems. For this reason we report the number of times the state and the adjoint equations are solved. In particular, in Table 6.1 we report the average number N_s and N_a over 10 time steps of evaluations of the state and the adjoint equations, for different initial guess of the Young modulus.

E_{guess}	10^4	10^5	10^6	10^7	10^8
$N_s \vert N_a$	8|8	5|5	3|2	4|4	6|4

TABLE 6.1

Convergence test. Average number of solutions over 10 time steps of the state and adjoint problem, for different initial guess of Young modulus.

Impact of noise. In order to take into account the presence of noisy data, we add a uniform noise $\boldsymbol{\nu}_P = P\, M\, \boldsymbol{\mathcal{U}}(-0.5, 0.5)$ (where M the maximum in space and time of the absolute value of displacement obtained by the forward simulation, and P and $\mathcal{U}$ as in Section 5.1) to the data coming from the forward simulation. At each time step we obtain different estimate for E, so we average them in order to obtain a unique estimate. We ran the optimization problem for 10 realizations of the noise. In Table 6.2, we report the average, over the 10 realizations, of the estimated values of E, the percentual errors and the number of times the state and the adjoint problems need

to be solved. Different initial guess for E and different percentage P are considered. These results show that the BFGS applied to the membrane case is quite robust with respect to the noise, both in term of accuracy and convergence. Moreover, it turns out that the values of E are estimated in excess. This suggests that the average in time we used to estimate E is polarized. However, a theoretical analysis of this aspect goes beyond the purposes of this work.

$\downarrow E_0 \setminus P \rightarrow$	0.1	0.2	0.3	0.4
$10^7\, dyne/cm^2$	1.302 ± 0.027	1.314 ± 0.054	1.330 ± 0.085	1.357 ± 0.103
	0.2% (4.7|3.0)	1.1% (4.5|3.2)	2.3% (4.6|3.11)	4.4% (4.5|3.0)
$10^5\, dyne/cm^2$	1.303 ± 0.027	1.315 ± 0.056	1.330 ± 0.087	1.348 ± 0.115
	0.2% (4.8|3.2)	1.1% (4.7|3.1)	2.3% (4.5|3.1)	3.7% (4.5|3.0)

TABLE 6.2

Noisy case. Mean and standard deviation of the ten estimates (to be multiplied by 10^6, top) and mean percentage error and number of state and adjoint solutions per iteration (bottom) for different values of the initial guess E_0 for the Young modulus and of the percentage P. Exact E is $1.3 \cdot 10^6\, dyne/cm^2$.

In Figure 6.2 is reported a comparison between the displacement of the forward simulation, the noisy data η_{meas} and the displacement recoverd with the estimated Young modulus. Despite the presence of noise, the estimated displacement mathces excellently the forward displacement.

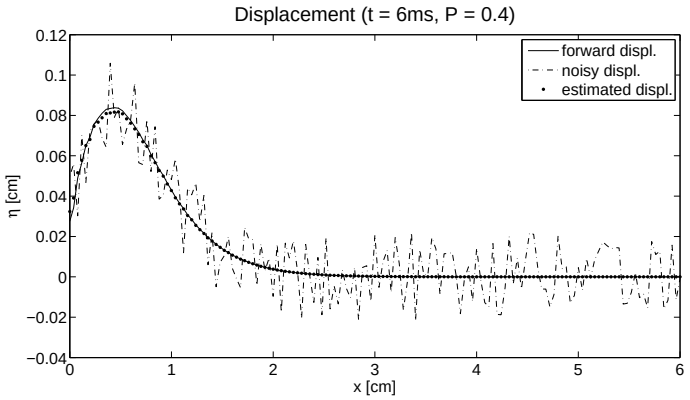

FIG. 6.2. *2d axisymmetric simulation on a tube. Comparison between the displacement obtained with the forward simulation, the noisy data and the computed displacement, at time $t = 6\ ms$ and for $P = 4$*

6.2.2. Numerical results on a simplified geometry representing an abdominal aneurysm. We consider a 2D axisymmetric geometry which represents an abdominal aneurysm (see Figure 6.3, top-left). The vessel membrane wall has been represented with a sinusoidal function. The radius of the vessel varies from 1 cm to 2.5 cm and the vessel length is 6 cm. We perform a synthetic simulation in which we prescribe the piecewise linear Young modulus shown in Figure 6.3 (bottom-left). Tipically, the aneurysm wall is stiffer than the healthy vessel wall (see e.g. [45]). Here, for the forward simulation, we take $E_a = 4 \cdot 10^6\, dyne/cm^2, E_b = 10^7\, dyne/cm^2, E_c = 5 \cdot 10^6\, dyne/cm^2$. We prescribe at the inlet a parabolic profile for the velocity, whose

maximum u_{max} lies on the axis of symmetry and it is given by

$$u_{max} = u^0_{max} + A \max\left\{\sin\left(\frac{2\pi t}{T}\right); 0\right\},$$

where $u^0_{max} = 5\ cm/s$, $A = 55\ cm/s$ and $T = 0.6\ s$. At the outlet we prescribe the absorbing Neumann boundary conditions porposed in [31]. We run the simulation for two "heart beat", i. e. for $0 < t \leq 2T$. As before, we add a uniform noise

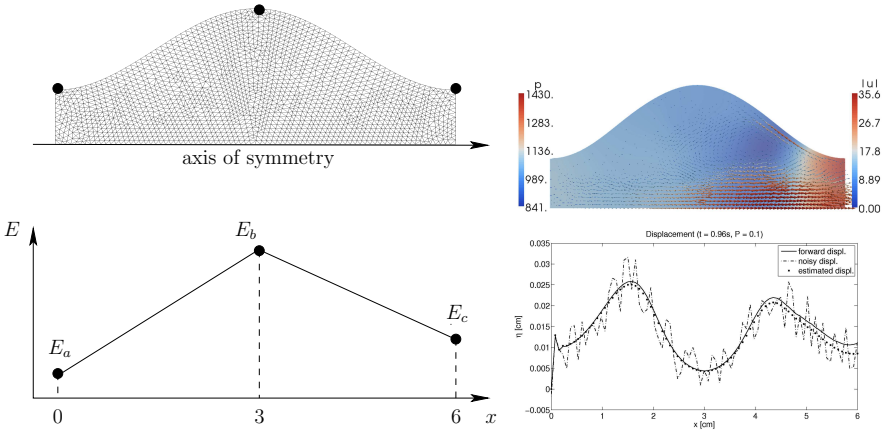

FIG. 6.3. *Aneurysm simulation. Top-left: mesh used for the simulation. Bottom-left: piecewise linear approximation of the Young modulus E in the forward simulation. Top-right: Velocity vectors and pressure at time $t = 0.96\ s$. Bottom-right: Comparison between the displacement obtained with the forward simulation, the noisy data and the computed displacement, at time $t = 0.96\ s$ and for $P = 0.1$.*

ν_P to the forward displacement η_{fwd} and we use the result as data for the control problem. As in the previous simulations, we average in time (during the second heart beat) the estimated values E^n_i. In Figure 6.3 (bottom-right) we report a comparison between the displacement obtained with the forward simulation, the noisy data and the computed displacement at time $t = 0.96\ s$. Again, the agreement is excellent.

In Table 6.3, we report the average, over the 10 realizations, of the estimated values of E_a, E_b and E_c and the number of times the state and the adjoint problem have needed to be solved. Different noise percentage P are considered. The initial gess is $E_{a,0} = E_{b,0} = E_{c,0} = 2 \cdot 10^7 dyne/cm^2$. The estimated values for $P = 0.1$ and $P = 0.2$ are quite accurate. For $P = 0.3$ the estimate of E_c is not feseable, hence has not been reported. To overcome this problem, we add to the functional the regularization term presented in Proposition 6, with $\xi = 2e-5$ and $E_{ref} = E_{a,0}$. Table 6.4 shows that the regularization term is effective. The esimates for E_c are still the more sensible to the noise, but now the estimated values are accettable. In the first time steps of the simulation, the forward displacements are very small for $x > 3\ cm$, hence the data is dominated by the noise in that region. This fact can be an explanation of the high sensibility to the noise of the estimated value for E_c.

This simplified model deserve further investigations. However, for the purpose of estimating the Young modulus, the membrane model could be a proper trade-off between accuracy and computational costs. This will be the subject of a future work.

	E_a	E_b	E_c	$iter.(state\|adjoint)$
$P = 0.1$	4.047 ± 0.118	10.19 ± 0.295	5.194 ± 0.240	12.9|3.5
	(1.2%)	(1.9%)	(3.9%)	
$P = 0.2$	4.034 ± 0.281	10.40 ± 0.505	5.507 ± 0.584	14.8|3.8
	(0.9%)	(4%)	(10%)	
$P = 0.3$	4.200 ± 0.550	10.89 ± 0.850	$-$	16.0|4.2
	(5%)	(8.9%)		

TABLE 6.3

Noisy case. Mean and standard deviation (to be multiplied by 10^6) of the ten estimates for E_a, E_b, E_c and number of state and adjoint iterations (bottom) for different values of the noise percentage P. The initial guess is $E_{a,0} = E_{b,0} = E_{c,0} = 2 \cdot 10^7 dyne/cm^2$.

	E_a	E_b	E_c	$iter.(state\|adjoint)$
$P = 0.1$	4.032 ± 0.119	10.15 ± 0.320	5.123 ± 0.129	13.1|3.7
	(0.8%)	(1.5%)	(2.5%)	
$P = 0.2$	4.222 ± 0.238	10.17 ± 0.510	5.349 ± 0.368	14.2|3.6
	(5.5%)	(1.7%)	(7.0%)	
$P = 0.3$	4.446 ± 0.426	10.57 ± 0.780	7.036 ± 3.90	15.5|4.1
	(11%)	(5.7%)	(41%)	
$P = 0.4$	4.386 ± 0.570	11.09 ± 1.519	7.802 ± 4.12	16.9|4.1
	(9.6%)	(11%)	(56%)	

TABLE 6.4

Noisy case with regularization term. Mean and standard deviation (to be multiplied by 10^6) of the ten estimates for E_a, E_b, E_c and number of state and adjoint iterations (bottom) for different values of the noise percentage P. The initial guess is $E_{a,0} = E_{b,0} = E_{c,0} = 10^7 dyne/cm^2$.

Acknowledgments. The third author has been partially supported by the ERC Advanced Grant N.227058 MATHCARD. The second author acknowledges the support of the EMORY URC project *Image Based Fluid-Structure Interaction Simulations in Computational Haemodynamics*.

REFERENCES

[1] S. BADIA, F. NOBILE, AND CH. VERGARA, *Fluid-structure partitioned procedures based on Robin transmission conditions*, Journal of Computational Physics , 227 (2008), pp. 7027–7051.

[2] P. E. BARBONE AND J. C. BAMBER, *Quantitative elasticity imaging: what can and cannot be inferred from strain images*, Physics in Medicine and Biology, 47 (2002), pp. 2147–2164. 575GM Times Cited:51 Cited References Count:26.

[3] J. M. BOESE, M. BOCK, S. O. SCHOENBERG, AND L. R. SCHAD, *Estimation of aortic compliance using magnetic resonance pulse wave velocity measurement*, Physics in Medicine and Biology, 45 (2000), pp. 1703–1713. PMID: 10870719.

[4] S.C. BRENNER AND L.R. SCOTT, *The mathematical theory of finite element methods*, Springer–Verlag, 1994.

[5] E. CASAS, *Optimal control in coefficients of elliptic equations with state constraints*, Applied Mathematics and Optimization, 26 (1992), pp. 21–37.

[6] P. CAUSIN, J.F. GERBEAU, AND F. NOBILE, *Added-mass effect in the design of partitioned algorithms for fluid-structure problems*, Computer Methods in Applied Mechanics and Engineering , 194(42-44) (2005), pp. 4506–4527.

[7] Z. CHEN AND J. ZOU, *An augmented lagrangian method for identifying discontinuous parameters in elliptic systems*, Siam J. Control Optim., 37 (1999), pp. 892–910.

[8] J.G. DEFARES AND M.E. WISE, *Theory of the measurement of arterial compliance in humans*, Bulletin of Mathematical Biology, 35 (1973), pp. 237–244.

[9] S. Deparis, M. Discacciati, G. Fourestey, and A. Quarteroni, *Fluid-structure algorithms based on Steklov-Poincaré operators*, Computer Methods in Applied Mechanics and Engineering , 195 (2006), pp. 5797–5812.
[10] J. Donea, *An arbitrary Lagrangian-Eulerian finite element method for transient dynamic fluid-structure interaction*, Computer Methods in Applied Mechanics and Engineering , 33 (1982), pp. 689–723.
[11] E. J. Topol (Eds.), *Textbook of Cardiovascular Medicine*, Lippincott-Raven Publisher, Philadelphia-New York, 1998.
[12] H.W. Engl, M. Hanke, and A. Neubauer, *Regularization of inverse problems*, Springer Netherlands, 1996.
[13] L. C. Evans, *Partial Differential Equations (Graduate Studies in Mathematics, V. 19) GSM/19*, American Mathematical Society, June 1998.
[14] M.A. Fernández, J.F. Gerbeau, and C. Grandmont, *A projection semi-implicit scheme for the coupling of an elastic structure with an incompressible fluid*, International Journal for Numerical Methods in Engineering , 69 (2007), pp. 794–821.
[15] B. Fischer and J. Modersitzki, *Ill-posed medicinean introduction to image registration*, Inverse Problems, 24 (2008), pp. 1–19.
[16] L. Formaggia, A. Quarteroni, and A. Veneziani (Eds.), *Cardiovascular Mathematics - Modeling and simulation of the circulatory system*, Springer, 2009.
[17] L. Formaggia, A. Veneziani, and C. Vergara, *Flow rate boundary problems for an incompressible fluid in deformable domains: formulations and solution methods*, Computer Methods in Applied Mechanics and Engineering , 199 (9-12) (2009), pp. 677–688.
[18] M. Galassi, J. Davies, J. Theiler, B. Gough, G. Jungman, M. Booth, and F. Rossi, *Gnu scientific library reference manual (3rd ed.)*, 2009.
[19] V. Girault and P.A. Raviart, *Finite element methods for Navier-Stokes equations*, Springer–Verlag, 1986.
[20] E.R. Giuliani, B.J. Gersh, M.D. McGoon, D.L. Hayes, and H.V. Schaff, *Mayor Clinic Practice of Cardiolgy*, Mosby Publisher, St.Luis, 1996.
[21] M. Gori and F. Maggi, *On the lower semicontinuity of supremal functionals*, Control, Optimisation and Calculus of Variations, 9 (2003), p. 9.
[22] M.D. Gunzburger, *Perspectives in flow control and optimization*, Society for Industrial Mathematics, 2003.
[23] G.A. Holzapfel, T.C. Gasser, and R.W. Ogden, *A new constitutive framework for arterial wall mechanics and a comparative study of material models*, Journal of elasticity, 61 (2000), pp. 1–48.
[24] F.C. Hoppensteadt and C.S. Peskin, *Modeling and simulation in medicine and the life sciences*, Springer Verlag, 2002.
[25] T. J. R. Hughes, W. K. Liu, and T. K. Zimmermann, *Lagrangian-Eulerian finite element formulation for incompressible viscous flows*, Computer Methods in Applied Mechanics and Engineering , 29 (1981), pp. 329–349.
[26] B. Jin and J. Zou, *Numerical estimation of the robin coefficient in a stationary diffusion equation*, IMA Journal of Numerical Analysis, 30 (2010), pp. 677–701.
[27] P.Y. Lagree, *An inverse technique to deduce elasticity of a large artery*, The European Phyisical Journal. Applied Physics., 9 (1999), pp. 153–163.
[28] V. Martin, F. Clment, A. Decoene, and J.-F. Gerbeau, *Parameter identification for a one-dimensional blood flow model*, Proceedings Cemracs, 14, pp. 174–200.
[29] M. Moubachir and J.P. Zolesio, *Moving Shape Analysis and Control: Applications to Fluid Structure Interactions*, Chapman & Hall/CRC, 2006.
[30] W. W. Nichols and M. F. O'Rourke, eds., *McDonald's Blood Flow in Arteries*, Hodder Arnold, 2005.
[31] F. Nobile and C. Vergara, *An effective fluid-structure interaction formulation for vascular dynamics by generalized Robin conditions*, SIAM J Sc Comp, 30 (2008), pp. 731–763.
[32] J. Nocedal and S. Wright, *Numerical Optimization*, Springer, Apr. 2000.
[33] A. A. Oberai, N. H. Gokhale, M. M. Doyley, and J. C. Bamber, *Evaluation of the adjoint equation based algorithm for elasticity imaging*, Physics in Medicine and Biology, 49 (2004), pp. 2955–2974. 848XA Times Cited:34 Cited References Count:34.
[34] A. A. Oberai, N. H. Gokhale, and G. R. Feijoo, *Solution of inverse problems in elasticity imaging using the adjoint method*, Inverse Problems, 19 (2003), pp. 297–313. 670TB Times Cited:47 Cited References Count:25.
[35] G. Odin, C. Savoldelli, P.o: Bouchard, and Y. Tillier, *Determination of young's modulus of mandibular bone using inverse analysis*, Medical Engineering and Physics, p. in press.
[36] B. M. Pannier, A. P. Avolio, H. Arnold, G. Mancia, and K. Takazawa, *Methods and*

devices for measuring arterial compliance in humans, America Journal of Hypertension, 15 (2002), pp. 743–753.

[37] K. Perktold and D. Hilbert, *Numerical simulation of pulsatile flow in a carotid bifurcation model*, Journal of biomedical engineering, 8 (1986), pp. 193–199.

[38] K. Perktold and G. Rappitsch, *Computer simulation of local blood flow and vessel mechanics in a compliant carotid artery bifurcation model*, Journal of Biomechanics, 28 (1995), pp. 845–856.

[39] K. Perktold, E. Thurner, and T. Kenner, *Flow and stress characteristics in rigid walled and compliant carotid artery bifurcation models*, Medical and Biological Engineering and Computing, 32 (1994), pp. 19–26.

[40] M. Piccinelli, L. Mirabella, T. Passerini, E. Haber, and A. Veneziani, *Image-based simulation of blood flow in deformable domains*. in preparation.

[41] S. Piperno and C. Farhat, *Partitioned prodecures for the transient solution of coupled aeroelastic problems-Part II: energy transfer analysis and three-dimensional applications*, Computer Methods in Applied Mechanics and Engineering , 190 (2001), pp. 3147–3170.

[42] A. Quarteroni, M. Tuveri, and A. Veneziani, *Computational vascular fluid dynamics: Problems, models and methods*, Computing and Visualisation in Science, 2 (2000), pp. 163–197.

[43] K. R. Raghavan and A. E. Yagle, *Forward and inverse problems in elasticity imaging of soft-tissues*, Ieee Transactions on Nuclear Science, 41 (1994), pp. 1639–1648. Part 1 Pe028 Times Cited:51 Cited References Count:18.

[44] W. Rudin, *Functional analysis*, McGraw-Hill series in higher mathematics, McGraw-Hill, New York,, 1973. 71039686 ocm00240184 (GUA)68542 24 cm. Bibliography: p. [384]-385. McGraw-Hill series in higher mathematics.

[45] A. R. Sekhri, W. R. Lees, and M. Adiseshiah, *Measurement of aortic compliance in abdominal aortic aneurysms before and after open and endoluminal repair: prelimiary results*, Journal of Endovasc. Ther., 11 (2004), pp. 472–482.

[46] N. Stergiopulos, J. J. Meister, and N. Westerhof, *Evaluation of methods for estimation of total arterial compliance.*, 1995.

[47] P. Le Tallec and J. Mouro, *Fluid structure interaction with large structural displacements*, Computer Methods in Applied Mechanics and Engineering , 190 (2001), pp. 3039–3067.

[48] T. Tonn, K. Urban, and S. Volkwein, *Optimal control of parameter-dependent convection-diffusion problems around rigid bodies*, Siam J. Sci. Comput., 32 (2010), pp. 1237–1260.

[49] S. N. Urchuk and D. B. Plewes, *A velocity correlation method for measuring vascular compliance using MR imaging*, Journal of Magnetic Resonance Imaging, 5 (1995), pp. 628–634.

[50] T. Washio, T. Hisada, H. Watanabe, and T.E. Tezduyar, *A robust preconditioner for fluid–structure interaction problems*, Computer Methods in Applied Mechanics and Engineering , 194 (2005), pp. 4027–4047.